28 October 2025

Independent evolution of holocentric chromosomes in an early branching apicomplexan parasite

Running title: Holocentricity in *Cryptosporidium*

Abigail Kimball[1#], Wanyi Huang[1#], Rui Xu[1,a], Melanie Key[1], Lisa Funkhouser-Jones[1,b], and L. David Sibley[1*]

[#] Contributed equally

Department of Molecular Microbiology, Washington University School of Medicine, St. Louis, MO 63110, USA

Present addresses:

[a] State Key Laboratory for Animal Disease Control and Prevention, South China Agricultural University, Guangzhou 510642, China

[b] Department of Microbial Pathogenesis & Immunology, Naresh K. Vashisht School of Medicine, Texas A&M University, Bryan, TX 77807, USA

*Address correspondence to Dr. L. David Sibley, Department of Molecular Microbiology, Washington University School of Medicine, 660 S. Euclid, CB 8230 St. Louis MO 63110. E-mail address: sibley@wustl.edu

Keywords: apicomplexan, mitosis, centromeres, holocentric, *Cryptosporidium*

ABSTRACT (150 limit)

During its asexual cycle, *Cryptosporidium parvum* (*C. parvum*) amplifies through three rounds of nuclear division before undergoing cytokinesis to form infectious merozoites. However, chromosome organization and segregation during nuclear division remain unstudied. Here, we visualized H3-histones, including the centromeric histone H3 (CENH3), telomeres, and centrosomes during mitosis. Nuclear division was accompanied by centriole duplication and elongated microtubules that spanned synchronously dividing nuclei. Surprisingly, *C. parvum* centromeres detected by CENH3 showed diffuse staining throughout nuclear division, that overlapped with telomeres at the apical nuclear end. Analysis of centromeres based on CENH3 capture and DNA sequencing revealed numerous distinct binding sites scattered across all eight chromosomes, including both coding regions and intergenic regions, that were typified by GA rich repeat sequences. The unique holocentric chromosome structure of *C. parvum* is unlike the single regional centromeres found in related apicomplexans, suggesting it arose independently from other known examples in plants, insects and worms.

INTRODUCTION

Cryptosporidium parvum (C. parvum), an obligate intracellular parasite, remains a serious global health and agricultural threat [1-4]. Transmission occurs through the ingestion of infectious oocysts and causes severe diarrheal illness in infants, young animals, and immunocompromised adults [5-7]. Once ingested, sporozoites exit the oocyst, invade host cells, and undergo three rounds of mitotic division within a single shared cytoplasm (the process of merogony), followed by cytokinesis to produce eight identical merozoites. Newly formed merozoites are released into the lumen, where they invade new host cells, and repeat the

47 invasion-egress cycle three times before transitioning to the sexual phase of the life cycle [8, 9].
48 Despite its significance as a global health problem, and the novelty of apicomplexan cellular
49 division processes, *C. parvum* mitosis remains largely uncharacterized, with our current
50 understanding limited to basic microscopy studies [8, 10-15].

51 To divide rapidly, apicomplexans have evolved mechanisms to streamline mitotic division.
52 Firstly, apicomplexans maintain their chromosomes in an uncondensed state, eliminating the
53 time-consuming steps of chromatin condensation and relaxation and allowing transcription to
54 resume quickly after division [16, 17]. This adaptation necessitates strict nuclear organization
55 during mitosis, where centromeres are typically maintained on the apical end of the nucleus
56 attached to the centrosome and telomeres persistently cluster at the basal end of the nuclear
57 periphery [18-20]. Additionally, apicomplexans maintain their nuclear envelope throughout
58 mitosis, minimizing the energy and time required for breakdown and reformation [17, 21]. A
59 consequence of this closed mitosis is restricted access of spindle fibers to chromosomes,
60 necessitating alternative segregation mechanisms. Rather than centrosomes orchestrating
61 microtubule organization from the cytoplasm, apicomplexan centrosome-like structures (spindle
62 pole bodies, microtubule-organizing centers) are embedded within the nuclear envelope and
63 serve as spindle assembly hubs that elongate the microtubules so they can attach to the
64 centromeres and ultimately coordinate chromosome movement during division [22-29]. Nuclear
65 pores are essential for nucleocytoplasmic transport through the intact envelope and directly
66 support the process of spindle assembly [30, 31]. Electron microscopy studies suggest that *C.*
67 *parvum* undergoes schizogony, with multiple rounds of nuclear replication preceding a
68 cytoplasmic division, followed by the egress of daughter parasites from the host cell. However, it

69 remains unclear whether *C. parvum* replicates its nuclei asynchronously, like *Plasmodium*, or
70 follows a more synchronized division like *Toxoplasma* [17, 32].
71 During mitosis and meiosis, centromeres function to orchestrate chromosome segregation
72 by serving as sites for microtubule anchoring to assure faithful separation at metaphase [33].
73 Centromeres have variable architecture in different organisms consisting of point centromeres
74 (small 250 bp single site per chromosome) in yeast [34], regional centromeres (gene poor islands
75 of heterochromatin ranging from several to hundreds of kb) in *T. gondii* and *P. falciparum* [26,
76 27, 35], and holocentric chromosomes (multiple centromere sites along the chromosome) found
77 in multiple species of plants, insects and worms [36-38]. Although centromere function is
78 essential and highly conserved across eukaryotes, centromeric DNA sequences and size are
79 subject to rapid evolution [39-41]. Variation in centromere architecture affects nuclear
80 organization, karyotype changes, and ultimately drives speciation [42, 43].
81 The nuclear structures, chromosome features, and mitotic mechanisms, including the role of
82 centromeres, have not been examined previously in *C. parvum*. Here, we delineate the
83 fundamental biology of *C. parvum* mitosis, revealing significant deviations from previously
84 assumed mechanisms. Using high-resolution imaging we examined nuclear division during the
85 first round of merogony, leveraging multiple transgenic parasite strains and mitosis-specific
86 antibodies. Additionally, we used Cleavage Under Targets and Nuclease Release (CUT&RUN)
87 [44] to identify the location of the centromeres based on CENH3 and patterns of centromere-
88 associated histone modifications in *C. parvum* and the related parasite *Toxoplasma gondii* (*T.*
89 *gondii*). In contrast to the monocentric centromeric structure of *T. gondii*, we found that *C.*
90 *parvum* has a dispersed centromeric chromosome structure with CENH3 binding sites scattered
91 across multiple small regions on all 8 chromosomes, resulting in diffuse CENH3 centromere

92 staining throughout mitosis. Overall, these results suggest that *C. parvum* employs a divergent
93 mitotic mechanism compared to other well-studied apicomplexans and has independently
94 evolved holocentric centromeres.
95
96 **RESULTS**
97 ***Characterization of centromeric histone H3 (CENH3) and histone H3 candidates in C.***
98 ***parvum***
99 The genome annotation of *C. parvum* contains two genes encoding Histone H3 *cgd3_2540* and
100 *cgd4_3220* (referred to here as H3.1 and H3.2, respectively) and a third gene *cgd4_2030*
101 annotated as a centromere-specific Histone H3 variant (CENH3). To validate these annotations,
102 we performed multiple BLASTP analyses using the protein products of each of these three *C.*
103 *parvum* genes to identify top hits in the following groups: 1) Apicomplexa (excluding all
104 *Cryptosporidium* species), 2) all eukaryotic organisms (excluding all Apicomplexa), 3) *Homo*
105 *sapiens*, and 4) *Saccharomyces cerevisiae.* Collectively, these analyses provide strong support
106 for cgd4_2030 as the CENH3 ortholog in *C. parvum* (**Table 1**). To examine the relationship
107 between the protein sequences for the *C. parvum* genes of interest and the top hits of BLASTP
108 analyses, a phylogenetic tree was generated (**Fig 1A**). We found that *cgd3_2540* (H3.1) and
109 *cgd4_3220* (H3.2) closely cluster with histone H3 sequences from other organisms, whereas
110 *cgd4_2030* (CENH3) clustered with other centromeric histone H3 proteins. We then directly
111 compared the amino acid sequences of H3.1 and H3.2 with a global sequence alignment and
112 found that the two sequences were highly similar (99.26%), but less similar compared to the
113 CENH3 (65.10% and 64.43%, respectively) (**Table 2 and Fig 1B**).

114 **Table 1:** The results of BLASTP analyses using the *C. parvum* centromeric histone H3-like protein (*cgd4_2030*), histone H3-like

115 proteins (*cgd3_2540* and *cgd4_3220).*

116

117 *

Query	Top hits in Apicomplexa*	E value	Top hits in all Eukaryotes#	E value	Top hits in *Saccharomyces cerevisiae*	E value	Top hits in *Homo sapiens*	E value
cgd4_2030	histone H3-like centromeric protein CSE4 [*C. cionae*]	5e-46	centromeric DNA-binding histone H3-like protein cse4 [*N. ribis*]	3e-39	Chain A, Cse4	2e-30	Chain A, Histone H3.1, Histone H3-like centromeric protein A, Histone H3.1	5e-39
cgd3_2540	histone H3 [*C. cionae*]	2e-86	histone H3-like [*P. hypophthalmus*]	3e-86	histone H3	4e-81	histone H3.2	1e-88
cgd4_3220	histone H3 [*C. cionae*]	2e-90	histone H3-like [*P. hypophthalmus*]	2e-87	histone H3	2e-81	histone H3.2	1e-89

118 *C.*

119 *parvum* proteins were compared against all organisms in the Apicomplexa phylum (except for *Cryptosporidium* spp.),

120 # *C. parvum* proteins were compared against all organisms (except for Apicomplexa)

121

122

123 **Table 2:** The identity and similarity results from multiple global sequence alignments between

124 H3.1, H3.2, and CENH3 proteins using a BLOSUM62 scoring matrix.

***Cp* H3.1 and *Cp* H3.2**	***Cp* CENH3 and *Cp* H3.1**	***Cp* CENH3 and *Cp* H3.2**
	Identity: 46.31% Similarity: 65.10% Gaps: 14.09%	
Identity: 97.78% Similarity: 99.26% Gaps: 0.00%		Identity: 46.31% Similarity: 64.43% Gaps: 14.09%

125

126 To further explore the distribution of H3.1 and H3.2 H3 variants, we generated two

127 transgenic lines of parasites that replaced the dispensable thymidine kinase (*tk*) gene with a

128 second copy of *cgd3_2540* (referred to as H3.1-3HA) or *cgd4_3220* (referred to as H3.2-3HA)

129 fused with a triple hemagglutinin (3HA) epitope tag using CRISPR/Cas9 (**Fig 1C, S1 A-B Fig,**

130 **Table S1**). Transgenic parasites were used to infect a human adenocarcinoma cell line (HCT-8)

131 monolayer, cultures were fixed at 18 hours post-infection (hpi) during merogony, stained, and

132 the localization of the 3HA tag was observed by immunofluorescence (IFA) high-resolution

133 confocal laser scanning microscopy equipped with Airyscan detection (LSCM-A). We found that

134 H3.1-3HA (**Fig 1D**) and H3.2-3HA (**Fig 1E**) had a diffuse staining pattern, which was expected

135 based on histone H3 staining in other apicomplexan parasites [27, 45, 46]

136

137 ***The staining pattern of C. parvum centromeric histone H3 (CENH3) is distinct.***

138 To visualize *C. parvum* centromeres, we used CRISPR-Cas9 gene editing to add a 3HA tag to

139 the C-terminus of the centromere-specific histone H3 variant protein (referred to as CENH3-

140 3HA) (**Fig 2A, S2 A-B Fig, Table S1**). After successfully selecting and amplifying these

141 transgenic parasites in immunocompromised mice, we infected HCT-8 cells for 22 h and

142 examined the staining pattern by LSCM-A microscopy. The CENH3 staining pattern observed in
143 *C. parvum* was unexpectedly highly diffuse and looked more like the pattern found in the H3.1-
144 3HA and H3.2-3HA tagged parasites (**Fig 2B-C**). The diffuse pattern of CENH3 staining in *C.*
145 *parvum* contrasts sharply with the regional centromeres previously described in *T. gondii* [27,
146 47]. Hence, we utilized a CENH3-3HA-tagged *T. gondii*, gifted by Dr. Kami Kim, as a staining
147 control for our experiments. These parasites were used for the infection of HCT-8 cells, fixed at
148 24 hpi, stained, and examined by high-resolution LSCM-A immunofluorescence (IFA)
149 microscopy (**Fig 2D-E)**. We found that the staining pattern of the centromeric histone H3 in *T.*
150 *gondii* is punctate, similar to what has been found previously in *T. gondii* by other investigators
151 [27, 47].

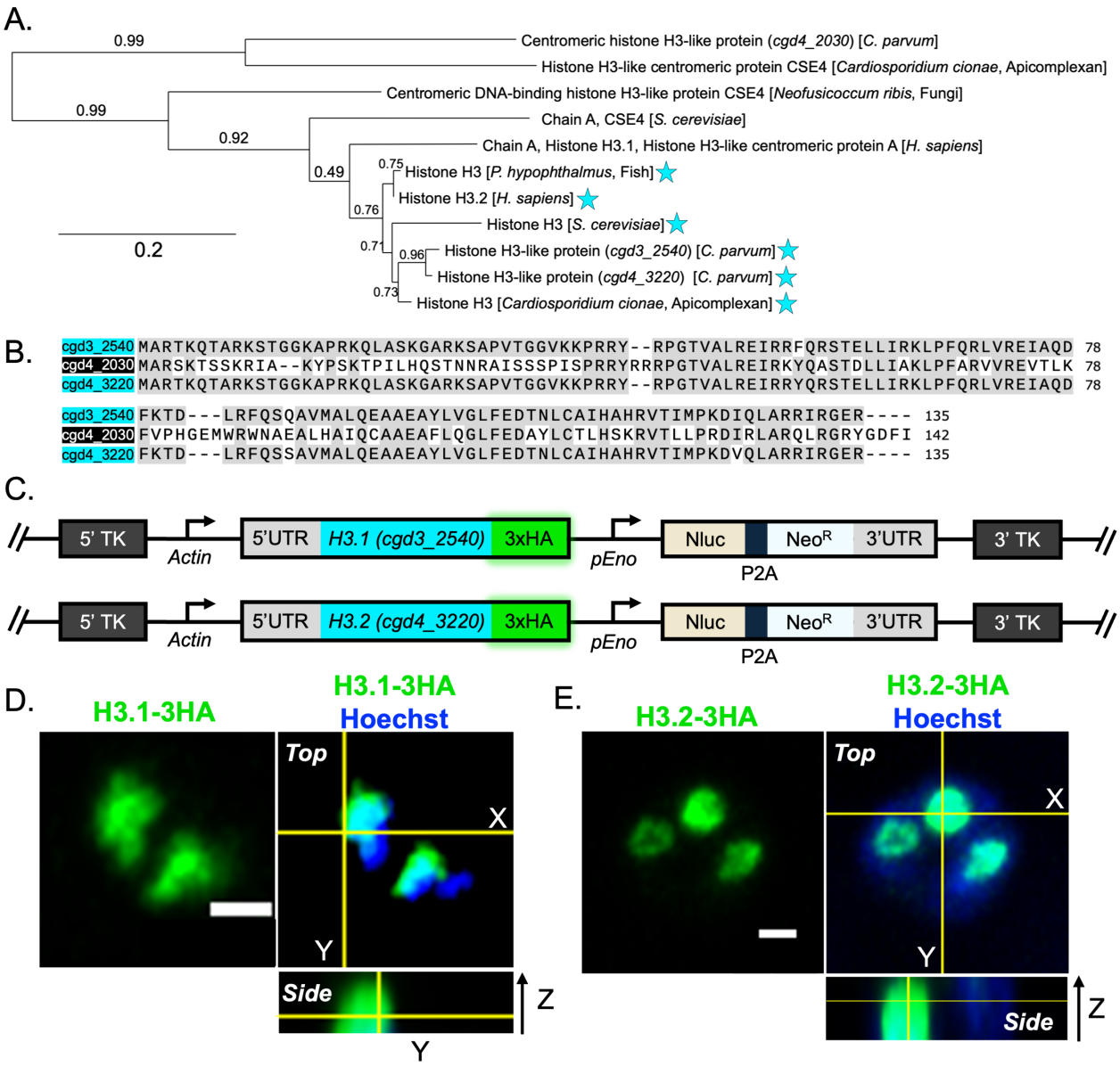

Figure 1: Characterization of centromeric histone H3 (CENH3) and histone H3 candidates in *C. parvum* and construction of Histone H3-3HA tagged strains. (A) Phylogenetic relationship of *C. parvum* H3 and centromeric H3 (CENH3) histones and their corresponding top BLASTP hits in other eukaryotes, apicomplexan parasites, *Saccharomyces cerevisiae*, or *Homo sapiens*. Cyan stars represent annotated histone H3 genes. (B) Protein sequence alignment of H3 (cyan) and CENH3 (black) in *C. parvum*. Amino acids that are identical between at least two sequences are highlighted in grey. (C) Diagram of the targeting constructs designed to replace

160 the endogenous *tk* locus with a second copy of either of the genes annotated as Histone H3-like
161 proteins in *C. parvum* (*cgd3_2540* or *cgd4_3220*), a 3HA tag, and a Nluc-P2A-NeoR cassette.
162 (D) Immunofluorescence staining of transgenic H3.1-3HA or (E) H3.2-3HA parasites. HCT-8
163 cells were infected with transgenic oocysts, fixed at 18 hpi, and stained with rat anti-HA and
164 VVL-Biotin, followed by secondary antibodies Alexa Fluor 488 goat anti-rat IgG and Alexa
165 Fluor 647 Streptavidin. Hoechst was used for nuclear staining. Images were acquired as Z-stacks
166 using a Zeiss LSM-880 Laser Scanning Confocal microscope equipped with Airyscan (LSCM-
167 A) and are presented with orthogonal views. Scale bars, 1 μm.
168
169 ***Mitosis is synchronous in C. parvum and centromeres remain diffuse.***
170 A vital step in mitosis is centrosome duplication, and previous studies in apicomplexans have
171 shown that it can be traced using antibodies that recognize the centrin 1 protein [27, 48]. A single
172 point adjacent to the nucleus occurs in non-replicating cells, while two centrin 1 positive points
173 per nucleus indicates the parasite is undergoing replication [27, 48]. In *Plasmodium*, during
174 schizogony, asynchronous duplications of centriolar plaques, structural equivalents of
175 centrosomes, have been observed across multiple nuclei within a single cytoplasm [28]. We
176 sought to identify centrosomes in *C. parvum* and determine whether its mitosis occurs
177 asynchronously, like *Plasmodium.* To identify parasites undergoing early mitosis, we infected
178 HCT-8 cells with excysted wild type *C. parvum* sporozoites, washed off uninvaded sporozoites
179 at 2 h, fixed the cultures at various timepoints between 6.5-8.5 hpi, and stained with Hoechst and
180 an anti-centrin-1 antibody. We found that, unlike *Plasmodium*, *C. parvum* appears to undergo
181 synchronized mitosis, as all nuclei within a dividing meront consistently exhibited two centrin-1
182 positive points per nucleus (**Fig 2F**). To determine if the diffuse centromere staining pattern

183 persisted during active mitosis in *C. parvum*, we infected cultures with CENH3-3HA parasites

184 and repeated the experiment previously described. We found that nuclei undergoing mitosis also

185 displayed a diffuse CENH3-3HA staining pattern by LSCM-A (**Fig 2G**). Despite

186 troubleshooting, we could not identify a signal in various CENH3-tagged lines using

187 ultrastructure expansion or immuno-electron microscopy, which may be due to the low

188 abundance of CENH3 and difficulty preserving the epitope.

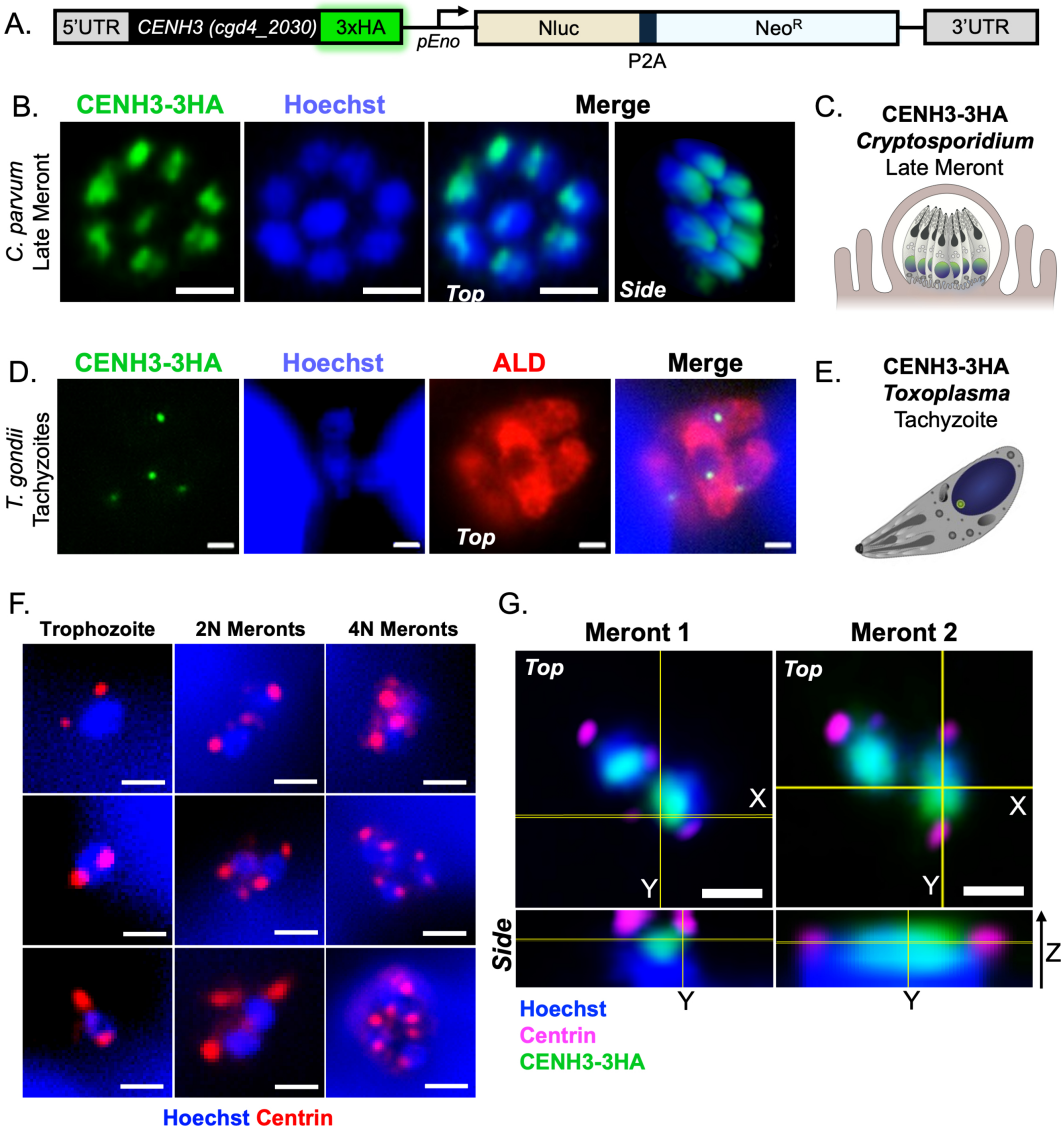

189

190 **Figure 2. The staining pattern of *C. parvum* centromeric histone H3 (CENH3) is distinct**

191 **from *Toxoplasma* and remains diffuse during mitosis.** (A) Diagram of the targeting construct

192 designed to add a 3HA tag and Nluc-P2A-Neo^{R} cassette to the C-terminus of the *C. parvum*
193 CENH3 (*cgd4_2030*). (B) HCT-8 cells were infected with CENH3-3HA *C. parvum* parasites,
194 fixed at 22 hpi, and stained with rat anti-HA and VVL-Biotin, followed by secondary antibodies
195 Alexa Fluor 488 goat anti-rat IgG and Alexa Fluor 647 Streptavidin followed by Hoechst
196 staining. Images were acquired as Z-stacks using LSCM-A and are presented with orthogonal
197 views. Scale bars, 1 µm. (C) Cartoon depiction corresponding to the microscopy image in panel
198 (B). In *Cryptosporidium*, a late-stage meront contains eight nuclei that have recently completed
199 cytokinesis to form mature merozoites. The CENH3-3HA signal within each nucleus displays a
200 diffuse staining pattern in *C. parvum*. (D) HCT-8 cells were infected with CENH3-3HA *T.*
201 *gondii* parasites, fixed at 24 hours post-infection (hpi), and stained with rat anti-HA and rabbit
202 anti-aldolase (ALD) to visualize the cytosol, followed by secondary antibodies Alexa Fluor 488
203 goat anti-rat IgG and Alexa Fluor 568 anti-rabbit IgG. Hoechst was used for nuclear staining.
204 Images were acquired as Z-stacks using LSCM-A and are presented with orthogonal views.
205 Scale bars, 1 µm. (E) Cartoon depiction corresponding to the microscopy image in panel (D). In
206 *T. gondii* tachyzoites, the CENH3-3HA signal within each nucleus displays a discrete staining
207 pattern. (F) HCT-8 cells were infected with excysted *C. parvum* sporozoites for 2 h, then washed
208 twice to remove extracellular parasites. Cultures were fixed at 30 min increments between 6-9
209 hpi to identify the first (trophozoites with one nucleus), second (early meronts with 2 nuclei), and
210 third (mid-stage meronts with 4 nuclei) mitotic divisions during the first round of merogony by
211 widefield microscopy. Scale bars, 1 µm. (G) Cultures were infected with CENH3-3HA *C.*
212 *parvum* sporozoites for 2 h, washed, and fixed at 6.5 hpi to capture the first round of mitosis.
213 Cultures were stained with rat anti-HA, rabbit anti-centrin-1, and VVL-Biotin, followed by
214 secondary antibodies Alexa Fluor 488 goat anti-rat IgG, Alexa Fluor 568 goat anti-mouse IgG,

215 and Alexa Fluor 647 Streptavidin, and lastly Hoechst. Parasites undergoing mitosis were
216 identified by having two centrin-1 points per nucleus, whereas parasites in interphase had only
217 one centrin-1 point. Images were acquired as Z-stacks using LSCM-A and are presented with
218 orthogonal views. Scale bars, 1 μm.
219
220 ***The telomere (G-strand binding protein, GBP) staining pattern is apical in C. parvum.***
221 G-quadruplex structures readily form at repetitive telomeric sequences and require G-quadruplex
222 binding proteins (GBPs) for stabilization (**Fig 3A**). A previous study identified *cgd1_3530* as the
223 GBP in *C. parvum* and determined the specific sequence necessary for *Cp*GBP binding
224 (GGTTA) [49]. Using AlphaFold and ChimeraX, we modeled the G-quadruplex structure
225 formed by this repetitive sequence and visualized how the *Cp*GBP protein interacts with and
226 stabilizes it. (**Fig 3B**). To identify the location of *C. parvum* telomeres relative to the
227 centromeres, we engineered transgenic parasites to express a 3HA tag at the gene encoding the
228 C-terminus of the G-quadruplex binding protein (referred to as GBP-3HA) (**Fig 3C, S2 A-B Fig,**
229 **Table S1**). Previous studies in *Plasmodium* have found that the telomeres are consistently found
230 on the opposite pole to the centromeres [50-52]. Since the centromeres were located at the apical
231 end of the nuclei in meronts, we expected that *C. parvum* telomeres would be at the basal end.
232 However, LSCM-A microscopy on infected HCT-8 monolayers (24 hpi) revealed that the
233 telomeres were also located at the apical side of the nucleus (**Fig 3D)**.
234
235 ***The telomere (GBP) and centromere (CENH3) staining patterns overlap in C. parvum.***
236 To confirm that *C. parvum* centromeres and telomeres had overlapping nuclear locations, we
237 generated an additional line of transgenic parasites that replaced the dispensable thymidine

238 kinase (*tk*) gene with a second copy of an N-terminally 3HA tagged CENH3 and GBP C-
239 terminally tagged with 3Ty via CRISPR/Cas9, with an intervening P2A split peptide to facilitate
240 co-expression of separate proteins (referred to as 3HA-CENH3-GBP-Ty) (**Fig 3E, S1C-D Fig,**
241 **Table S1)**. HCT-8 cultures were infected with 3HA-CENH3-GBP-Ty parasites, fixed at 6.5 hpi,
242 and examined by LSCM-A microscopy after staining. We confirmed that 3HA-CENH3 and
243 GBP-3Ty staining overlapped completely on the apical end of the nucleus (visualized by
244 Hoechst) (**Fig 3F)**.
245

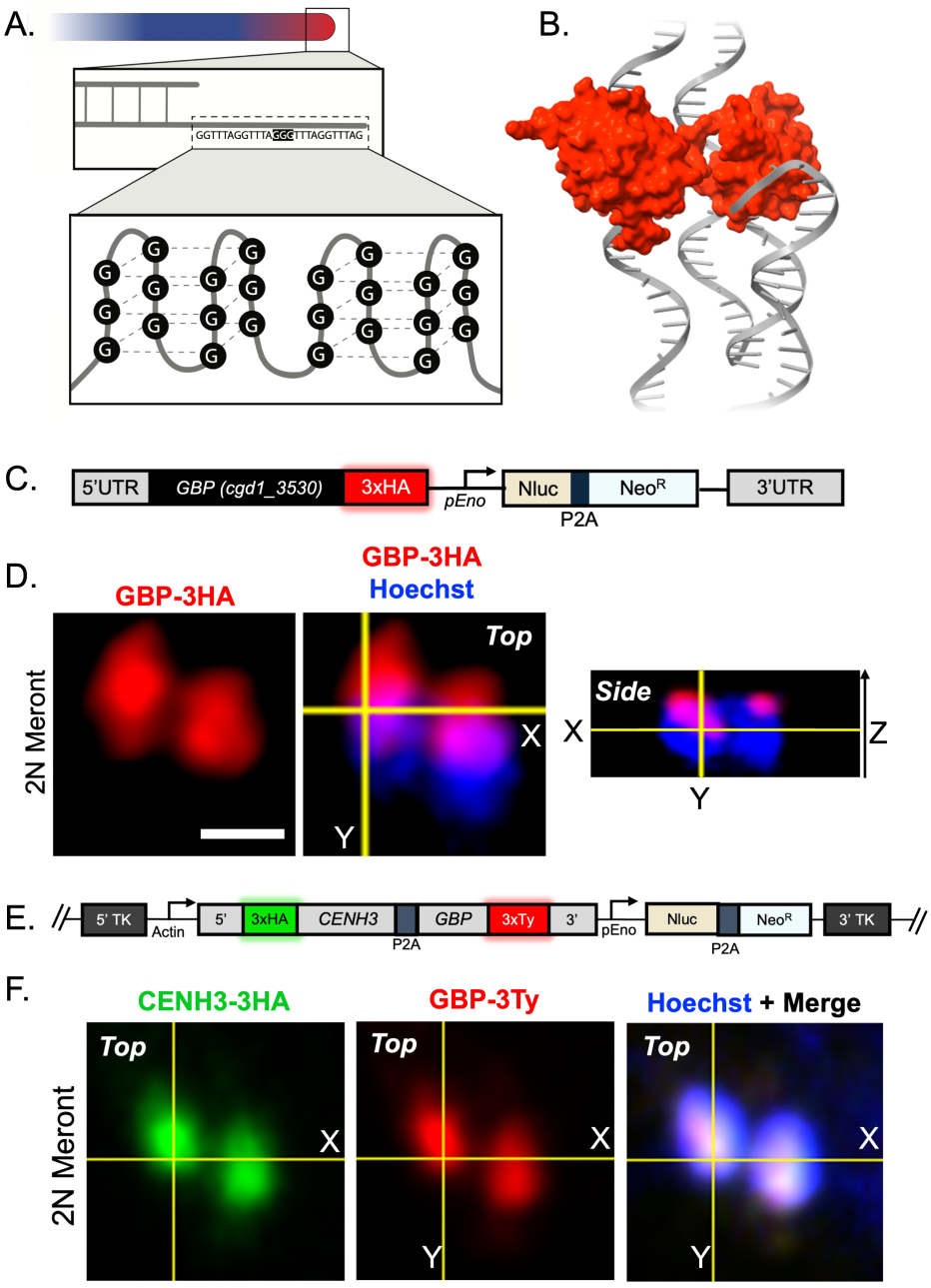

Figure 3: The telomere (G-strand binding protein, GBP) staining pattern is apical in *C. parvum* and overlaps with the centromere (CENH3) staining pattern. (A) The 3' overhang single-stranded DNA at the end of telomeres contains repetitive sequences $(GGTTTA)_n$ in *C. parvum* that form G-quadruplex structures. (B) The G-quadruplex binding protein (GBP) is essential for forming and stabilizing these structures. The sequence of *Cp*GBP and its binding motif has been previously determined and the protein structure is modeled by Alphafold and

253 ChimeraX [49]. (C) Diagram of the targeting construct designed to add a 3HA tag and Nluc-
254 P2A-Neo^R cassette to the C-terminus of the G-quadruplex binding proteins gene *(*GBP*,*
255 *cgd1_3530)* (D) HCT-8 cells were infected with GBP-3HA parasites, fixed at 6.5 hpi to capture
256 early meronts (2 nuclei), and stained with rat anti-HA and VVL-Biotin, followed by secondary
257 antibodies Alexa Fluor 488 goat anti-rat IgG and Alexa Fluor 647 Streptavidin. Hoechst was
258 used for nuclear staining. Images were acquired as Z-stacks using LSCM-A and are presented
259 with orthogonal views and the scale bar is 1 µm. (E) Diagram of the targeting construct designed
260 to replace the endogenous *tk* locus with a second copy of CENH3 N-terminally tagged with 3HA
261 and GBP with a C-terminal 3xTy tag separated with a P2A split peptide. (F)
262 Immunofluorescence staining of transgenic 3HA-CENH3-GBP-3Ty parasites. HCT-8 cells were
263 infected with transgenic oocysts, fixed at 6.5 hpi to capture early meronts (2 nuclei), and stained
264 with rat anti-HA, mouse anti-Ty, and VVL-Biotin followed by a secondary antibody stain
265 containing Alexa Fluor 488 goat anti-rat IgG, Alexa Fluor 568 goat-anti mouse, and Alexa Fluor
266 647 Streptavidin. Hoechst was used for nuclear staining. Images were acquired as Z-stacks using
267 LSCM-A and are presented with orthogonal views. Scale bars, 1 µm.
268
269 ***Detection of mitotically active DNA, microtubules, and the nuclear pore proteins in C. parvum***
270 The phosphorylation of histone H3 (specifically at serine 10 and serine 28) is a highly conserved
271 mechanism for initiating chromosome condensation in preparation for mitosis [53]. Antibodies
272 recognizing the phosphorylated version of H3 at serine 10 are commonly used in other systems
273 to determine which cells are currently undergoing mitosis from late interphase through telophase
274 [54]. Even though apicomplexan parasites are known not to condense their chromosomes, *C.*
275 *parvum* meronts frequently stained positive for the phosphorylated histone H3 (PH3) antibody

276 (**Fig 4A**). Furthermore, PH3 positive parasites also contained nuclei with duplicated centrin-1
277 positive centrosomes, suggesting that it provides a marker of mitotic parasites. We visualized
278 nuclear pores in *C. parvum* with an antibody that recognizes NUP116 in *Plasmodium falciparum*
279 *(P. falciparum)* and found that it reliably stained the parasite nucleus in a punctate pattern that
280 was concentrated primarily peripherally in the nucleus (**Fig 4B**). Among apicomplexan parasites,
281 mitosis has primarily been studied in *T. gondii* and *P. falciparum* [16, 17, 27, 55]. These studies
282 demonstrate that once centrosomes duplicate, and the nuclear envelope forms a tunnel-like
283 structure, organizing spindle microtubules within it. As the tunnel progressively perforates,
284 spindle microtubules access the centromere, attaching to mediate chromosome movement [32].
285 This process was visualized in *C. parvum* by staining with antibodies that recognize the centrin-1
286 and alpha tubulin (**Fig 4C-D**). We frequently observed two conformations of centrin-1 tubulin
287 structures that may correlate with early (**Fig 4C**) and late mitotic phases (**Fig 4D**). Early in
288 mitosis, the microtubules are relatively short and form a straight line (**Fig 4C, E**). Later, they are
289 accompanied by a wider nucleus, have elongated, and form a "v" shape, suggesting they have
290 attached to the chromosomes and are mediating their movement before budding (**Fig 4D, F**).

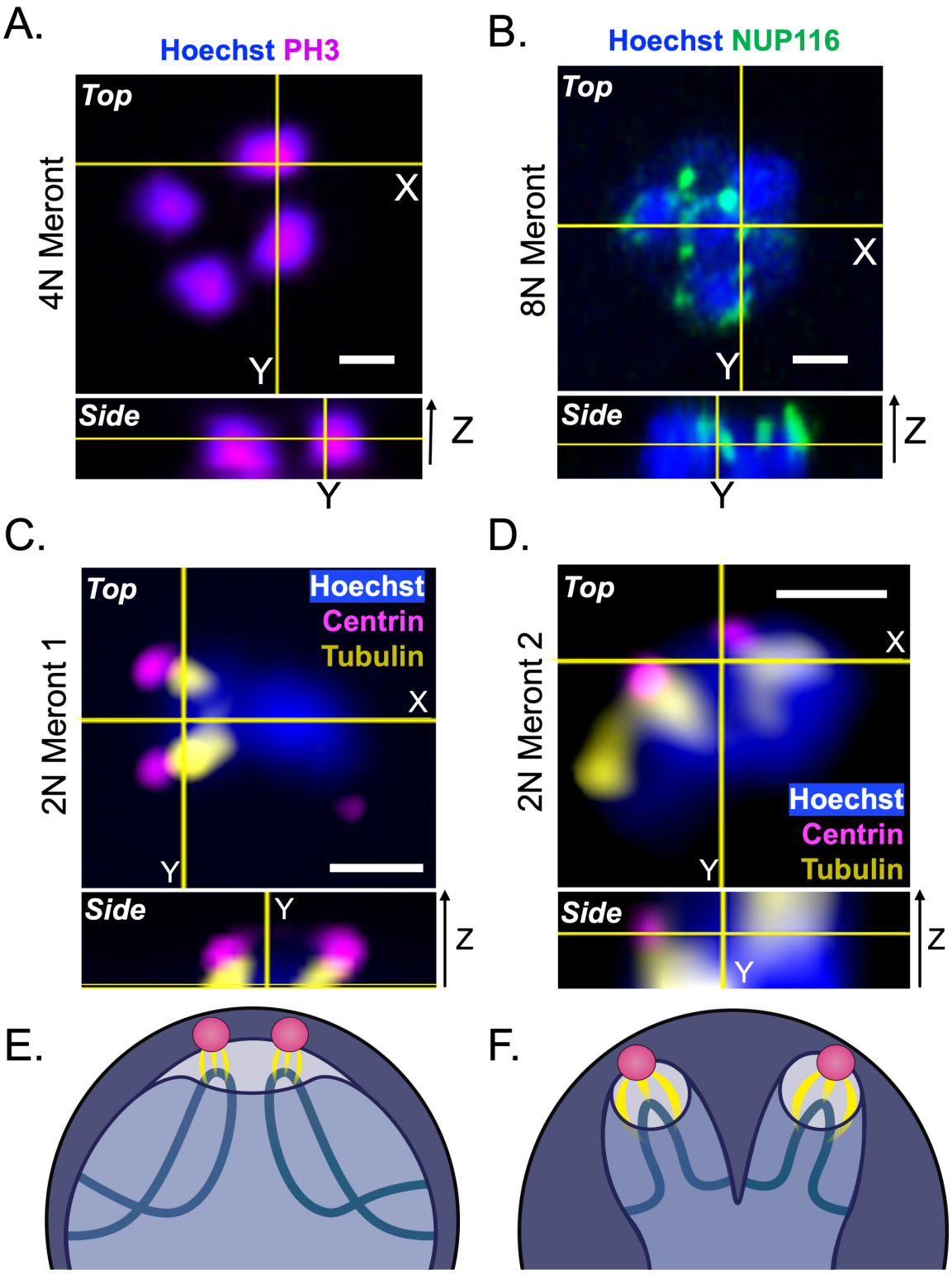

291

292 **Figure 4: Mitotically active DNA, microtubules, and the nuclear pore proteins as visualized**

293 **by antibody staining in *C. parvum*.** (A) HCT-8 cells were infected with wild type parasites,

294 fixed at 18 hpi, and stained with rabbit anti-phosphorylated Histone H3 (PH3) followed by an
295 Alexa Fluor 568 goat anti-rabbit IgG antibody. DNA was stained with Hoechst and a mid-stage
296 meront with 4 nuclei is shown. (B) Parasites were prepared identically to panel A, but were
297 stained with an antibody that recognizes a subunit of the nuclear pore in *Plasmodium falciparum*
298 (NUP116) followed by an Alexa Fluor 568 goat anti-rabbit IgG antibody and Hoechst. A late-
299 stage meronts with 8 nuclei is shown. (C, D) HCT-8 cells were infected with wild type parasites,
300 fixed at 6.5 hpi to capture early meronts (2 nuclei), and stained with rabbit anti-centrin-1, mouse
301 anti-tubulin, and VVL-Biotin, followed by the secondary antibodies Alexa Fluor 488 goat anti-
302 mouse IgG, Alexa Fluor 568 goat anti-rabbit IgG, Alexa Fluor 647 Streptavidin, and Hoechst.
303 The nucleus in the first meront (C) is likely an example of early mitosis, whereas the second
304 meront (D) is likely an example of a later phase of the mitotic process. Images were acquired as
305 Z-stacks using LSCM-A and are presented with orthogonal views. Scale bars, 1 μm. (E) A
306 cartoon representation of the mitotic structures visualized in (C). The pink circles represent
307 centrin, which is localized to the intact nuclear envelope. Yellow microtubules originate from the
308 centriole-equivalent structures and attach to the uncondensed chromosomes visualized by
309 Hoechst. (F) A cartoon representation of the mitotic structures visualized in (D). Later in mitosis,
310 the microtubules (yellow) become more prominent and the centriole-equivalent structures (pink)
311 move away from one another, indicating active segregation and preparation for cytokinesis.
312
313 ***Composition of centromeres in C. parvum and T. gondii***
314 Centromeres are defined by the deposition of CENH3-containing nucleosomes [27, 56]. Given
315 the diffuse staining of CENH3, we wanted to further characterize the centromere by identifying
316 DNA sites bound by this protein. Therefore, we adopted protocols for CUT&RUN to identify

317 centromeres based on CENH3 binding based on capture with anti-HA antibody in *C. parvum*
318 [44]. To ensure sufficient HA binding, we developed a CENH3 line tagged with spaghetti
319 monster (referred to as CENH3-smHA) that contains 10 HA epitope repeats for these
320 experiments and validated identical staining patterns to CENH3-3HA *C. parvum* (**S2 A-C Fig,**
321 **Table S1**). To validate our experimental strategy, we first applied CUT&RUN to *T. gondii*,
322 whose centromeres have previously been defined by ChIP-seq [27]. Our CUT&RUN data
323 closely matched earlier findings, with CENH3 enrichment observed at discrete chromosomal loci
324 corresponding to the previously described centromeres (**Fig 5A, S3A-C Fig**). We also detected
325 the positive correlation of CENH3 with H3K9me3 and inverse correlation with H3K4me3
326 reported in earlier ChIP-chip analyses (**Fig 5A, S3A-B Fig**). Based on these signals, we
327 implemented a stepwise strategy to identify centromeric regions. Valleys in H3K4me3,
328 consisting of 20 kb windows, sized to match reported centromere lengths (16 kb ± 3.4 kb)[27],
329 combined with co-enrichment of H3K9me3 with CENH3-smHA were used as criteria for
330 identifying centromere regions (**S3D Fig**). Applying these rules, we identified a single
331 centromere in each of the 13 chromosomes of *T. gondii* (**S3E Fig**), with Chr VIIb identified as
332 part of Chr VIII [57](**S3C Fig**).
333 We next applied CUT&RUN to *C. parvum*. Initial experiments using a 120-minute MNase
334 digestion failed to generate usable data, as both sequencing depth and genome coverage were
335 low compared to negative controls (**S1 Dataset**). Since CENH3 nucleosomes can be
336 hypersensitive to MNase digestion, as reported previously in *Caenorhabditis elegans* (*C.*
337 *elegans)* [56], we tested digestion times of 5, 30, and 60 min. The 30 min digestion yielded the
338 best coverage and sequencing depth, and these conditions were used for following analyses (**S1**
339 **Dataset, S4A Fig**). Unlike *T. gondii*, read mapping profiles for CENH3 in *C. parvum* showed

340 signals broadly distributed along chromosomes (**Fig 5B**). To locate centromeric regions in *C.*
341 *parvum*, we first attempted the *T. gondii* stepwise strategy, but no valid windows were detected.
342 As the CENH3 distribution resembled that of the holocentric nematode *C. elegans*, we adjusted
343 thresholds accordingly by restricting the peaks analysis to 400 bp windows (**S4B Fig**). We
344 identified 423 CENH3-enriched regions distributed across all chromosomes. Heatmaps and
345 aggregate signal profiles showed that these windows displayed features of CENH3 enrichment
346 correlated with H3K9me3 deposition and H3K4me3 depletion, suggesting that they represent
347 centromere-associated chromatin (**S4C-D Fig**). Importantly, these signals were largely absent in
348 wild type parasites stained with HA antibody as a control, supporting their authenticity (**S4C-D**
349 **Fig**). To further refine localization, we excluded windows overlapping with WT-HA signals,
350 reducing the dataset to 347 high-confidence centromeric windows (**S4B,E Fig**). Taken together,
351 these results indicate that *C. parvum* possesses many small CENH3 binding sites dispersed
352 across eight chromosomes, in contrast to the monocentric nature of *T. gondii*.
353 We further investigated characteristics of *C. parvum* centromeres. In contrast to *T. gondii*,
354 where centromeres are typically located within large intergenic regions [27], no extended
355 intergenic regions were observed in *C. parvum* due to the tight compaction of the genome.
356 Surprisingly, the majority of *C. parvum* CENH3-associated windows were located within gene
357 coding regions rather than being restricted to intergenic regions (**S2 DataSet2**). To determine
358 whether centromeric regions were also present within intergenic regions of *C. parvum*, we
359 applied a stepwise identification strategy using a slightly relaxed read depth threshold (**S4F Fig**).
360 We identified 58 centromeric regions distributed within intergenic regions across all
361 chromosomes (**Fig. 5C, S3 DataSet**). Heatmaps and aggregate signal profiles for CNEH3 as well
362 as chromatin marks also supported that they represent centromere-associated chromatin (**Fig.**

363 **5D,E**). These results suggest that CENH3 binding in *C. parvum* is broadly distributed throughout
364 the chromosomes, including both with in coding regions and intergenic regions. To assess
365 sequence properties of *C. parvum* centromeric windows, motif analysis of *C. parvum*
366 centromeric windows was performed using MEME, revealing two GA-rich motifs enriched at
367 CENH3-associated sites (**Fig 5F**). Notable, these GA repeats are also found in other regions of
368 the genome that were not identified in the CENH3 capture studies.

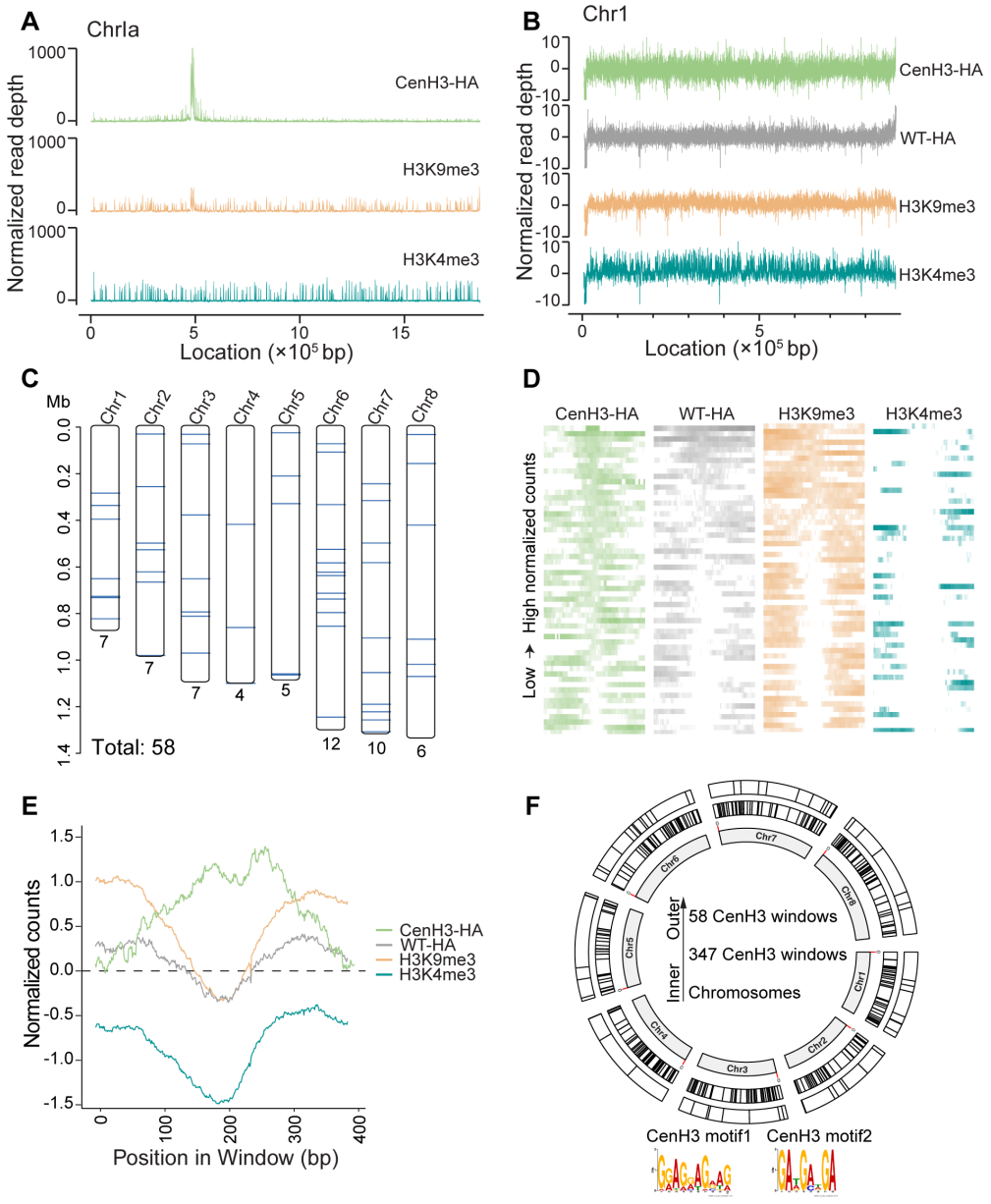

369

370 **Figure 5. Genome-wide distribution of CENH3 in *Toxoplasma gondii* and *Cryptosporidium***
371 ***parvum***. (A) Genome browser view of *T. gondii* chromosome Ia showing CUT&RUN signals for
372 CENH3-HA (HA antibody), H3K9me3, and H3K4me3. CENH3 signal enrichment positively
373 correlates with H3K9me3 and inversely with H3K4me3. Peaks of CENH3 enrichment are
374 indicated (red arrows). (B) Genome browser view of *C. parvum* chromosome I, showing
375 CUT&RUN signals for CENH3-HA *C. parvum* captured with HA antibody and wild type *C.*
376 *parvum* captured with HA antibody (referred to as WT-HA), H3K9me3, and H3K4me3
377 (captured with antibodies). (C) Chromosomal distribution of the 58 CENH3-enriched windows
378 in intergenic regions of *C. parvum* chromosomes (Chr#). Numbers below each chromosome
379 indicate the number of windows. (D) Heatmaps of CUT&RUN signals for the groups shown in
380 (B) within a 400 bp window around all 58 CENH3-enriched windows . Each row represents an
381 individual centromeric site, ranked by signal intensity. (E) Average signal profiles for CENH3-
382 HA (green), WT-HA (gray), H3K9me3 (orange), and H3K4me3 (teal) across the 400 bp window
383 around CENH3 sites. (F) Circos plot of CENH3-associated motifs. From inner to outer rings:
384 chromosomes, locations of 347 CENH3-enriched windows found in coding regions (black), and
385 locations of 58 CENH3-enriched windows found in intergenic regions (black). Representative
386 sequence logos for motif 1 and motif 2 are shown.
387
388 **DISCUSSION**
389 Despite rapid asexual proliferation being required for parasite expansion, the molecular
390 mechanisms that underlie *C. parvum* mitosis have remained unexplored. To investigate this
391 process, we examined nuclear division using markers to track multiple rounds of mitosis during
392 merogony. Nuclear division in *C. parvum* occurs synchronously as shown by staining with

393 phospho-H3 and centrin-1, which provide markers for mitotically active chromatin and
394 duplicating centrosomes, respectively. Surprisingly, both CENH3, a marker for centromeres, and
395 GBP, a marker for telomeres, were diffusely localized across the apical half of the nucleus.
396 Moreover, these diffuse apical patterns persisted throughout mitosis, as shown by tracking
397 nuclear division through stages visualized with centrin-1 and microtubules. To explore the
398 molecular nature of centromeres, we performed CUT&RUN sequencing of transgenic parasites
399 expressing epitope-tagged CENH3. Although discrete monocentric peaks were detected in the
400 related parasite *T. gondii*, CENH3 binding sites were diffusely scattered across ~ >400 sites in
401 the *C. parvum* genome. Overall, these findings indicate that *C. parvum* has evolved an alternative
402 chromosome structure compared to other apicomplexan parasites, differences that may have
403 significant functional consequences for chromosome stability and meiotic recombination.
404 Following entry of sporozoites (or merozoites) into the host cell, the parasite undergoes
405 merogony, consisting of 3 rounds of nuclear division prior to cytokinesis to generate infectious
406 merozoites. By tracking nuclear division with phospho-H3, to detect mitotically active nuclei,
407 and centrin-1 to monitor dividing centrosomes, we observed that all nuclei found in a common
408 cytoplasm shared the same centrin-1 staining pattern (whether dividing or not), indicating that
409 nuclei divide synchronously. This pattern differs from *Plasmodium* schizogony, where nuclei are
410 observed at different mitotic stages within a single schizont [28]. In *Plasmodium*, nuclear pores
411 are important for cell division as they facilitate the transport of mitotic molecules through the
412 intact nuclear envelope and associate with the centriolar plaques [31, 58]. Although we did not
413 examine the dynamics of nuclear pores during division, they appear as peripheral puncta in
414 mature meronts and may serve a similar function in *C. parvum*. Staining with alpha-tubulin
415 allowed us to visualize *C. parvum* microtubules during mitosis, particularly at early stages where

416 it spanned dividing nuclei, likely representing extra-nuclear spindles involved in chromosome
417 separation. By monitoring the duplication of the centrosomes, distance between the centrin-1
418 foci, length of microtubules, and elongation of the nucleus we generated a pseudo timeline for
419 early, mid, and late merogony. These findings provide an important foundation for studies of the
420 dynamics of centromere staining described below.

421 Unexpectedly, we found a diffuse nuclear CENH3-3HA staining pattern rather than the
422 punctate pattern observed in other apicomplexan parasites [27, 29, 35]. We also confirmed that
423 the diffuse CENH3 staining pattern did not deviate when the method of tagging was altered (e.g.
424 GFP, mNeon, and smHA), when the location of the tag was swapped (C vs N-terminally tagged),
425 or when a tagged second copy of the gene was inserted into a neutral locus of the genome. We
426 also developed epitope-tagged lines of telomere-binding protein GBP, similar to studies in
427 *Eimeria* and *Plasmodium* [59, 60]. Unlike in other apicomplexans, GBP also showed an apical
428 location in *C. parvum*, overlapping closely with CENH3 [18-20, 50]. We further confirmed that
429 the telomeres and centromeres occupied a similar nuclear location using a parasite strain in
430 which CENH3 and GBP proteins were simultaneously expressed as tagged second copies. This
431 pattern contrasts sharply with other apicomplexans where telomers are localized to the opposite
432 pole of the nucleus from centromeres [50-52]. We sought to determine if centromeres remained
433 diffuse throughout mitosis by simultaneously visualizing the centriole-equivalent structures and
434 centromeres by staining CENH3-3HA with anti-HA and centrin-1 antibodies. We confirmed that
435 in *C. parvum,* the diffuse centromere staining pattern does not change throughout mitosis, which
436 further contrasts with the highly focal nature of centromeres in *T. gondii* and *P. falciparum* [26,
437 27].

438 Given the highly unusual staining patterns of CENH3 in *C. parvum*, we decided to
439 investigate CENH3 binding sites on DNA using CUT&RUN sequencing. For comparison, we
440 also performed CUT&RUN studies on CENH3 in the related parasite *T. gondii* and compared
441 them to previous studies that used ChIPSeq to define centromeres [27]. In *T. gondii*, CUT&RUN
442 sequencing identified highly similar CENH3 binding sites to those reported previously by
443 ChIPSeq [27] with a single predominant peak on each chromosome, including newly defined
444 peaks on chromosome IV, that had not been identified previously. Centromeres in *T. gondii*
445 consist of gene-poor regions of ~15 kb that are not defined by any particular sequence or repeats
446 but instead are positively correlated with H3K9me3 and inversely correlated with H3K4me3,
447 typical chromatin patterns expected for centromeric regions [18, 27]. Under similar conditions,
448 CUT&RUN experiments for CENH3 binding sites in *C. parvum* failed to identify similar
449 singular dominant peaks on each chromosome. Instead, CENH3 binding sites were
450 hypersensitive to MNase digestion, with the signal being the highest at a 30- min incubation
451 time, similar to that observed in ChIP-seq studies of the holocentric nematode *Caenorhabditis*
452 *elegans* (*C. elegans*) [56]. Under optimal digestive conditions, we found that the CENH3 signal
453 in *C. parvum* was broadly distributed along chromosomes, with ~ 350 distinct sites in coding
454 regions and another ~ 60 sites within intergenic regions scattered across 8 chromosomes.
455 Interestingly, like *T. gondii*, *C. parvum* CENH3 peaks also correlated with H3K9me3 signal and
456 were found in areas lacking H3K4me3, consistent with a centromere-associated chromatin
457 pattern. The distribution of CENH3 binding sites in *C. parvum* is similar to that described in *C.*
458 *elegans* as polycentric, implying that CENH3 binds to distinct sites rather than diffusely across
459 the entire chromosome [56].

460 Collectively, our findings are consistent with *C. parvum* containing holocentric centromeres
461 based on the following criteria: Firstly, the staining pattern of CENH3 diffusely stains the apical
462 half of the nucleus under nondividing conditions, in contrast to the focal staining of CENH3 in *T.*
463 *gondii* [18, 27] and *P. falciparum* [26]. Secondly, the diffuse pattern of CENH3 staining remains
464 throughout mitosis, suggesting centromeres do not coalesce into a single regional center. Thirdly,
465 CENH3 binding sites as defined by CUT&RUN resemble the dispersed pattern of low-intensity
466 peaks seen in *C. elegans*, which has well-characterized holocentric chromosomes. Finally, the
467 CENH3 binding sites show evidence of simple GA nucleotide repeats, a feature also seen in *C.*
468 *elegan*s [56]. In both cases, the GA repeats are also found in other regions of the respective
469 genomes, so this feature alone is not sufficient to mediate CENH3 binding. One unusual feature
470 of the CENH3 binding sites in *C. parvum* is that they extend into coding regions, which is not an
471 expected feature of centromeres. The dispersed polycentric pattern of CENH3 binding sites in *C.*
472 *elegans* is also unusual in that these regions are concentrated in High Occupancy Targets (HOT)
473 sites for permissive binding of transcription factors [56]. In *C. elegans*, the CENH3 and HOT
474 sites appear to serve a dual purpose: in replicating cells they bind CENH3, while they recruit
475 transcription factors when CENH3 is lost during exit from the cell cycle in differentiated muscle
476 cells [56]. By analogy, transcriptional silencing during mitosis in *C. parvum* may allow CENH3
477 binding in coding regions to facilitate chromosome segregation, with displacement during the
478 rest of the cell cycle when transcription is active. Alternatively, the CENH3 binding sites in
479 intergenic regions may function as the primary centromere localizing signal for formation of
480 kinetochores.
481 Holocentric chromosomes have been documented in many species, primarily through direct
482 cytological observation, yet their functional implications and evolutionary origins remain poorly

483 understood [38, 56, 61, 62]. Current evidence suggests that holocentric chromosomes have
484 evolved convergently at least 13 times across distantly related taxa in both the plant and animal
485 kingdoms [37, 38, 62]. Holocentricity has not previously been described in protists, and hence it
486 likely evolved independently in *C. parvum*. It is also possible that holocentricity is more
487 widespread among protists but that it has been overlooked due to their small size and failure to
488 condense chromosomes during division. One proposed advantage of holocentricity is its capacity
489 to stabilize chromosomal fragments during mitosis, thereby mitigating genetic loss. This trait
490 may confer a selective benefit to organisms frequently exposed to elevated levels of DNA
491 damage due to environmental stressors or lifestyle factors [37, 61]. Thus, holocentricity may
492 impart genome stability under stress encountered in the gastrointestinal system where the
493 parasite is exposed to toxic bacterial metabolites [63] and host immune responses [64]. Despite
494 this potential advantage, holocentricity also presents a major challenge for coordinating
495 chromosome segregation following crossover during meiosis I. Well-characterized holocentric
496 species have evolved mechanisms to circumvent this issue, such as inverted meiosis or, in the
497 case of *C. elegans*, the deployment of kinetochore proteins that localize to discrete chromosomal
498 regions, effectively mimicking monocentric behavior [65]. Whether *C. parvum* uses a similar
499 mechanism as *C. elegans* to localize kinetochore proteins to discrete sites on the chromosome is
500 uncertain, but previous work from our laboratory examining crossover rates during *C. parvum*
501 meiosis revealed a high frequency of crossover events and failed to find evidence for inverted
502 meiosis, a process used by some holocentric organisms [66].

503 **Limitations and Future Studies**

504 Examination of the nuclear organization of *C. parvum* throughout the cell cycle revealed a
505 persistently diffuse centromere staining pattern, suggesting a holocentric chromosome structure.

506 During division, such multiple centromeric sites dispersed along the chromosome are expected to
507 bind centrosomes and thereby connect to microtubules for chromosome separation. Although we
508 visualized events consistent with this process in an artificial timeline, future studies using
509 fluorescent reporters could potentially provide more precise information on the formation of
510 centrosomes, coordinated assembly of microtubules, and nuclear division in *C. parvum*.
511 However, obtaining direct cytological data in support of holocentric centromeres and their
512 behavior during nuclear division will be challenging in this system because chromosomes do not
513 condense during division. Alternatively, it may be possible to explore the nature of centromeres
514 by examining the distribution of other conserved centrosome and kinetochore binding proteins
515 during nuclear division. Such studies could shed further light on chromosome tethering in
516 nuclear division and provide invaluable insights into unique evolutionary adaptations in *C.*
517 *parvum*.
518
519 **Acknowledgements:**
520 We thank Jennifer Barks for assistance with cell culture, Dr. Wandy L. Beatty, Microbiology
521 Imaging Facility, Washington University School of Medicine in St. Louis, for assistance with
522 microscopy, and Dr. Kami Kim, Univ. South Florida, for providing the *T. gondii* CENH3-HA
523 line used here. We are grateful for helpful comments from Drs. Daniel E Goldberg, Douglas L.
524 Chalker, and Tim Schedl, Washington University and Dr. Lihua Xiao, South China Agricultural
525 University. Genome sequencing was performed by the GTAC Genome core at Washington
526 University in St Louis. Supported in part by the Graduate Research Fellowship Program,
527 National Science Foundation (to A.K.) and grant AI175150 from the National Institutes of
528 Health (to L.D.S.).

529

530 **Author contributions**

531 AK: Conceptualization, Data curation, Formal analysis, Funding acquisition, Investigation,
532 Methodology, Resources, Validation, Visualization, Writing – original draft, Writing – review &
533 editing

534 WH: Data Curation, Formal analysis, Investigation, Methodology, Resources, Visualization,
535 Writing

536 MK: Investigation, Methodology, Resources

537 LFJ: Investigation, Methodology, Resources

538 LDS: Conceptualization, Funding acquisition, Methodology, Project administration, Resources,
539 Supervision, Validation, Writing – original draft, Writing – review & editing

540

541 **Data Sources and Availability:**

542 All materials described here are available from the corresponding author based on MTA.
543 Sequence for the CUT&RUN analyses have been deposited to the NCBI Bioproject #
544 PRJNA1330822.

545 **Declarations:**

546 The authors declare that they have no conflicts to disclose.

547

548 **MATERIALS & METHODS**

549 **Animal studies and ethical approval.**

550 Animal studies were approved by the Institutional Animal Studies Committee (School of
551 Medicine, Washington University in St. Louis). *Ifngr1*$^{-/-}$ mice (003288; Jackson Laboratories),

552 and NOD scid gamma mice (referred to as NSG) (005557; Jackson Laboratories) were bred in-
553 house in a specific-pathogen-free animal facility on a 12:12 light-dark cycle. Male and female
554 mice between 8 and 12 weeks of age were used for sex-matched groups used in crossing
555 experiments. Mice were co-housed with siblings of the same sex throughout the experiments.
556 **Cell culture.**
557 HCT-8 cells (Human ileocecal adenocarcinoma, ATCC CCL-244) derived from a human
558 ileocecal carcinoma were cultured in RPMI 1640 ATCC Modification medium supplemented
559 with 10% fetal bovine serum at 37 °C in a 5% CO_2 incubator. After trypsinization, 450,000 cells
560 were plated on glass coverslips in 24-well plates and used for experiments. Cells were confirmed
561 to be mycoplasma-free with the e-Myco plus Mycoplasma PCR detection kit.
562 **Immunofluorescence assays & microscopy.** Staining protocols have been previously described
563 and all antibodies are listed in **Table S2** [67]. Briefly, infected HCT-8 cultures were fixed with
564 4% formaldehyde 8-24 hours post-infection (hpi), permeabilized with 0.1% Triton X-100,
565 blocked with 1% bovine serum albumin (BSA), stained with a primary antibody mixture for 1 h
566 followed by secondary antibodies for 1 h and Hoechst for 20 min. Primary antibodies were
567 diluted for staining: anti-HA (rat, 1:500), VVL-Biotin (*Vicia Villosa* Lectin, Biotinylated, 1:500),
568 anti-Aldolase (ALD, rabbit, 1:1000) centrin-1 (mouse, 1:250), anti-Ty (mouse, 1:250), and anti-
569 PH3 (rabbit, 1:500). All Alexa Fluor secondary antibodies were diluted at 1:1000 and Hoechst
570 was diluted 1:2000. Coverslips were mounted onto microscope slides with Prolong Glass
571 Antifade Mountant. Coverslips were visualized using a Zeiss LSM880 laser scanning confocal
572 microscope equipped with a 63x, 1.4 N.A. Zeiss Plan Apochromat oil objective lens and Airy
573 scan. Images were acquired with ZEN v2.1, v2.5 software and further analyzed using ImageJ.
574

575 **CRISPR/Cas9 plasmid construction.**

576 ***Plasmid construction***

577 Primers used to generate the following plasmids were ordered from IDT and all sequences are
578 found in **Table S3**. SnapGene (v7.1.1) and NEBuilder Assembly Tool (v2.9.0) were used to
579 construct plasmid maps and design primers.

580 The CENH3-3HA tagging plasmid was generated using the previously described ABC-3HA
581 tagging plasmid [68] by replacing the C-terminal and 3'UTR sequences with equivalent regions
582 from the *Cp*CENH3 gene amplified from *C. parvum* cDNA to generate the tagging plasmid
583 CENH3-3HA-Nluc-P2A-Neo^{R}.

584 The 3HA-CENH3- GBP-3Ty tagging plasmid was created via a seven-way Gibson assembly
585 combining a backbone generated from the TK-GFP-Nluc-P2A-Neo^{R}-TK homology tagging
586 plasmid previously generated in our lab [69] together with the following fragments: 1) The 5'
587 homology region of CENH3 (500 bp), the CENH3 CDS, a portion of the 3' homology region of
588 CENH3 (216 bp) were amplified from the CENH3-3HA tagging plasmid described above. 2)
589 The 3HA-pLinker region was amplified from a TK-3HA-CENH3-Nluc-P2A-Neo^{R}-TK plasmid
590 (data not shown in this study), 3) the GBP CDS was amplified from *C. parvum* genomic DNA,
591 4) the pLinker-3Ty sequence was amplified from a tagging plasmid previously generated in our
592 lab [68], and 5) the P2A skip peptide sequence was generated as a gBlock Gene Fragment from
593 Azenta. The U6:sgTK plasmid previously generated in our lab was utilized for all experiments
594 with TK locus replacement repair plasmids [69].

595 The H3.1-3HA and H3.2-3HA tagging plasmids were generated via Gibson assembly using
596 the 3HA-CENH3-GBP-3Ty plasmid to provide a backbone, the pLinker-3HA region was

597 amplified from the CENH3-3HA tagging plasmid described above, and the CDS regions for
598 H3.1 and H3.2 were amplified from *C. parvum* genomic DNA.
599 The GBP-3HA tagging plasmid was generated using the CENH3-3HA tagging plasmid
600 described above for the backbone and replacing the C-terminal and 3'UTR sequences with the
601 GBP CDS sequence amplified from *C. parvum* genomic DNA.
602 CENH3 and GBP CRISPR/Cas9 plasmids were created via Gibson assembly of the
603 linearized backbone amplified from the TK CRISPR/Cas9 plasmid (Addgene 122852) and an
604 oligonucleotide with the sgRNA specific for the CENH3 or GBP gene [69]. The Eukaryotic
605 Pathogen CRISPR guide RNA/DNA Design tool (http://grna.ctegd.uga.edu) was used to identify
606 CENH3 and GBP sgRNA sequences.
607 **Amplifying transgenic parasites in mice.**
608 The transfection and amplification of parasites in immunocompromised mice were conducted as
609 previously described [69-72]. Briefly, $1x10^8$ freshly excysted sporozoites were electroporated
610 with 100 µg of repair plasmid and 66 µg of CRISPR/Cas9 plasmid, then resuspended in 300 µL
611 of cold DPBS. *Ifngr1*$^{-/-}$ mice were first orally gavaged with an 8% (wt/vol) sodium bicarbonate
612 solution to neutralize stomach acid, followed by the administration of the electroporated
613 sporozoites. To facilitate the selection of transgenic parasites, paromomycin (16 g/L) was
614 provided in the drinking water 24 h post-infection. Fecal pellets were collected at intervals post-
615 infection for luciferase assays and diagnostic PCR analysis to verify parasite growth and proper
616 gene insertion. Oocysts were isolated from fecal material using bleach treatment, and 20,000
617 oocysts per mouse were employed for a subsequent round of amplification in NSG mice.
618 **Luciferase assays for mouse experiments.** Fecal samples collected from infected mice were
619 analyzed with the Promega Nano-Glo luciferase assay kit, as previously described [72]. The

620 luciferase activity was measured using the BioTek Cytation 3 cell imaging multi-mode reader.
621 The number of relative luminescence units per milligram of feces was obtained by dividing the
622 average values from two technical replicates by the fecal sample weight.

623 **Quantifying oocyst shedding in mouse experiments.** DNA was extracted from fecal pellets
624 collected from infected mice using the QIAamp PowerFecal DNA kit, following previously
625 established methods [69, 71, 72]. Quantitative PCR (qPCR) analysis was conducted to determine
626 the number of oocysts at each time point based on *C. parvum* glyceraldehyde-3-phosphate
627 dehydrogenase (GAPDH) primers and a standard curve derived from a dilution series (**S2 Table**)
628 [69]. Genomic DNA (gDNA) amounts were quantified using the QuantStudio 3 real-time PCR
629 system.

630 **Confirmation of insertions in transgenic parasites by PCR.**
631 To confirm the correct integration of the homology repair template, extracted gDNA from
632 murine fecal samples and wild type controls were used as the template. PCR amplification was
633 performed using 1 µL of the extracted gDNA, Q5 Hot Start high-fidelity 2X master mix or
634 PrimeSTAR GXL premix (TaKaRa), and primers at a final concentration of 500 nM on a Veriti
635 96-well thermal cycler. All PCR products were resolved on a 1% agarose gel containing GelRed
636 (1:10,000) and visualized using the ChemiDoc MP imaging system.

637 **Oocyst purification from fecal material and storage.**
638 The *C. parvum* isolate AUCP -1 used for transfections was purified from fecal material collected
639 from male Holstein calves at the University of Illinois at Urbana-Champaign [73]. All
640 procedures involving the calves received approval from the Institutional Animal Care and Use
641 Committee (IACUC). Transgenic oocysts were purified in-house from fecal material collected
642 from NSG mice, using a saturated sodium chloride solution for oocyst flotation [74]. Post-

643 purification, oocysts were stored at 4°C in phosphate-buffered saline (PBS) for up to three
644 months following fecal collection.

645 **Structural predictions**

646 The protein structure of the G-quadruplex binding protein (GBP, *cgd1*_3530) was predicted
647 using Alphafold 3 (www.alphafoldserver.com). Using ChimeraX
648 (https://www.cgl.ucsf.edu/chimerax/), we modeled how the G-quadruplex structure formed by
649 the *Cp*GBP repetitive binding sequence (GGTTA) [49] interacts and is stabilized by the CpGBP
650 protein.

651 **Parasite Preparation and Lysis for CUT&RUN experiments.**

652 The CENH3-3HA line of *T. gondii* [27] was obtained from the laboratory of Dr. Kami Kim at
653 University of South Florida. *Tg*CENH3-3HA tachyzoites were propagated in human foreskin
654 fibroblasts and harvested using established protocols [75]. *C. parvum* sporozoites ($4x10^7$) and *T.*
655 *gondii* tachyzoites ($1x10^7$) were centrifuged at 2,500 RPM for 5 min, supernatants removed, and
656 parasites were resuspended in 2 mL of cold parasite lysis buffer (10 mM HEPES pH 7.9, 1.5 mM
657 MgCl2, 10 mM KCl, 0.65% NP40 (supplemented with IGEPAL) and 0.5 mM PMSF
658 (supplemented with cOmplete EDTA free protease inhibitor cocktail and sterile distilled H_2O),
659 incubated for 10 min on ice, and centrifuged at 3,000 RPM for 10 min at 4°C (previously
660 described in [76, 77]).

661 **CUT&RUN Processing, Library Preparation, Quality Control & Sequencing.**

662 Following lysis treatment, the lysis buffer was removed, and the nuclei pellet was washed
663 following the CUT&RUN Kit Version 4 protocol (EpiCypher, Inc, Catalog No. 14-1048).
664 Isolated nuclei were incubated with either 1.0 µg of rat anti-HA antibody, 0.5 µg of rabbit anti-
665 H3K4me3 positive control antibody, or 0.5 µg of mouse anti-IgG negative control antibody.

666 Chromatin digestion and release steps were performed according to the EpiCypher protocol, and
667 5 ng of CUT&RUN enriched DNA was used for library preparation according to the CUT&RUN
668 Library Prep Kit User Manual Version 1.5 (EpiCypher, Inc, Catalog No. 14-1001). The
669 concentrations of CUT&RUN library samples were determined via Qubit and quality control
670 were assessed with an Agilent 4200 TapeStation.

671 **CUT&RUN Analysis & Visualization.**

672 Multiple CUT&RUN runs were preformed to obtain biological replicates of each sample. DNA
673 products were sequenced on an Illumina NovaSeq 6000 using 150-bp paired-ends at the GTAC
674 sequencing core at Washington University in St. Louis. Sequence reads obtained from Illumina
675 were trimmed for adapter sequences and poor sequence quality (phred score < 25 and trimmed
676 length < 50) using fastp v0.23.4. The trimmed reads were mapped to the reference *C. parvum*
677 IOWA-CDC genome using BWA-MEM v0.7.17 [78]. Duplicate reads were marked and
678 removed in the bam files using the MarkDuplicates algorithm of picard v3.1.1
679 (https://broadinstitute.github.io/picard/) with REMOVE_DUPLICATES=true,
680 CREATE_INDEX=true, and ASSUME_SORTED=true. Reads with mapping lengths less than
681 50 bp were further removed from the bam files using SAMtools v1.7
682 (http://samtools.sourceforge.net/). Genome coverage and sequence depth were estimated using
683 the mpileup algorithm of SAMtools. The read depth of each locus was normalized by dividing by
684 the total number of counts for all loci, then scaled by multiplying by the number of loci in the
685 genome. Input counts were subtracted from negative control counts. Data was visualized by a R
686 package 'ggplot2' (https://www.rdocumentation.org/packages/ggplot2). Motifs within
687 centromeric windows were identified using MEME v5.5.8 (https://meme-
688 suite.org/meme/tools/meme). Chromosomal distributions of intergenic regions, centromeric

689 windows, and motifs were visualized with Circos plot generated in TBtools-II v2.311

690 (https://github.com/CJ-Chen/TBtools-II).

691

692 **REFERENCES:**
693

694 1. Tyzzer E. An extracellular coccidium, Cryptosporidium muris (gen. et sp. nov.), of the
695 gastric glands of the common mouse. J Med Res. 1910;23:487-509. PubMed Central
696 PMCID: PMCPMC2098948.
697 2. Greenberg PD, Koch J, Cello JP. Diagnosis of Cryptosporidium parvum in patients with
698 severe diarrhea and AIDS. Dig Dis Sci. 1996;41(11):2286-90.
699 3. Striepen B. Parasitic infections: Time to tackle cryptosporidiosis. Nature.
700 2013;503(7475):189-91. PubMed Central PMCID: PMC24236315.
701 4. Tzipori S, Widmer G. A hundred-year retrospective on cryptosporidiosis. Trends Parasitol.
702 2008;24(4):184-9. Epub 20080307. doi: 10.1016/j.pt.2008.01.002. PubMed PMID:
703 18329342; PubMed Central PMCID: PMCPMC2716703.
704 5. Sow SO, Muhsen K, Nasrin D, Blackwelder WC, Wu Y, Farag TH, et al. The Burden of
705 Cryptosporidium Diarrheal Disease among Children < 24 Months of Age in
706 Moderate/High Mortality Regions of Sub-Saharan Africa and South Asia, Utilizing Data
707 from the Global Enteric Multicenter Study (GEMS). PLoS Negl Trop Dis.
708 2016;10(5):e0004729. Epub 2016/05/25. doi: 10.1371/journal.pntd.0004729. PubMed
709 PMID: 27219054; PubMed Central PMCID: PMCPMC4878811.
710 6. Kotloff KL, Nataro JP, Blackwelder WC, Nasrin D, Farag TH, Panchalingam S, et al. Burden
711 and aetiology of diarrhoeal disease in infants and young children in developing countries
712 (the Global Enteric Multicenter Study, GEMS): a prospective, case-control study. Lancet.
713 2013;382(9888):209-22.
714 7. Wanyiri JW, Kanyi H, Maina S, Wang DE, Steen A, Ngugi P, et al. Cryptosporidiosis in
715 HIV/AIDS patients in Kenya: clinical features, epidemiology, molecular characterization
716 and antibody responses. Am J Trop Med Hyg. 2014;91(2):319-28. Epub 2014/05/29. doi:
717 10.4269/ajtmh.13-0254. PubMed PMID: 24865675; PubMed Central PMCID:
718 PMCPMC4125256.
719 8. Funkhouser-Jones LJ, Ravindran S, Sibley LD. Defining Stage-Specific Activity of Potent
720 New Inhibitors of Cryptosporidium parvum Growth In Vitro. mBio. 2020;11(2). Epub
721 2020/03/05. doi: 10.1128/mBio.00052-20. PubMed PMID: 32127445; PubMed Central
722 PMCID: PMCPMC7064746.
723 9. English ED, Guerin A, Tandel J, Striepen B. Live imaging of the Cryptosporidium parvum
724 life cycle reveals direct development of male and female gametes from type I meronts.
725 PLoS Biol. 2022;20(4):e3001604. Epub 2022/04/19. doi: 10.1371/journal.pbio.3001604.
726 PubMed PMID: 35436284; PubMed Central PMCID: PMCPMC9015140.
727 10. Beyer TV, Svezhova NV, Sidorenko NV, Khokhlov SE. Cryptosporidium parvum (Coccidia,
728 Apicomplexa): Some new ultrastructural observations on its endogenous development.
729 European Journal of Protistology. 2000;36(2):151-9. doi: 10.1016/s0932-4739(00)80034-
730 6.
731 11. Pohlenz J, Bemrick WJ, Moon HW, Cheville NF. Bovine cryptosporidiosis: a transmission
732 and scanning electron microscopic study of some stages in the life cycle and of the host-
733 parasite relationship. Vet Pathol. 1978;15(3):417-27. Epub 1978/05/01. doi:
734 10.1177/030098587801500318. PubMed PMID: 98896.
735 12. Tzipori S, McCartney E, Lawson GH, Rowland AC, Campbell I. Experimental infection of
736 piglets with cryptosporidium. Res Vet Sci. 1981;31(3):358-68. Epub 1981/11/01.
737 PubMed PMID: 7342229.

738 13. Current WL, Reese NC. A comparison of endogenous development of three isolates of
739 Cryptosporidium in suckling mice. J Protozool. 1986;33(1):98-108. Epub 1986/02/01.
740 PubMed PMID: 3959014.
741 14. Keithly JS, Langreth SG, Buttle KF, Mannella CA. Electron tomographic and ultrastructural
742 analysis of the Cryptosporidium parvum relict mitochondrion, its associated membranes,
743 and organelles. J Eukaryot Microbiol. 2005;52(2):132-40. Epub 2005/04/09. doi:
744 10.1111/j.1550-7408.2005.04-3317.x. PubMed PMID: 15817118.
745 15. Wilke G. Development of an in vitro Culture System for Cryptosporidium parvum. Theses
746 and Dissertations: Washington University in St. Louis; 2020.
747 16. White MW, Suvorova ES. Apicomplexa Cell Cycles: Something Old, Borrowed, Lost, and
748 New. Trends Parasitol. 2018;34(9):759-71. Epub 20180802. doi:
749 10.1016/j.pt.2018.07.006. PubMed PMID: 30078701; PubMed Central PMCID:
750 PMCPMC6157590.
751 17. Striepen B, Jordan CN, Reiff S, van Dooren GG. Building the perfect parasite: cell division
752 in apicomplexa. PLoS Pathog. 2007;3(6):e78. doi: 10.1371/journal.ppat.0030078.
753 PubMed PMID: 17604449; PubMed Central PMCID: PMCPMC1904476.
754 18. Gissot M, Walker R, Delhaye S, Huot L, Hot D, Tomavo S. Toxoplasma gondii
755 chromodomain protein 1 binds to heterochromatin and colocalises with centromeres and
756 telomeres at the nuclear periphery. PLoS One. 2012;7(3):e32671. Epub 20120309. doi:
757 10.1371/journal.pone.0032671. PubMed PMID: 22427862; PubMed Central PMCID:
758 PMCPMC3302879.
759 19. Duraisingh MT, Voss TS, Marty AJ, Duffy MF, Good RT, Thompson JK, et al.
760 Heterochromatin silencing and locus repositioning linked to regulation of virulence genes
761 in Plasmodium falciparum. Cell. 2005;121(1):13-24. doi: 10.1016/j.cell.2005.01.036.
762 PubMed PMID: 15820675.
763 20. del Cacho E, Pages M, Gallego M, Barbero JL, Monteagudo L, Sanchez-Acedo C. Meiotic
764 chromosome pairing and bouquet formation during Eimeria tenella sporulation. Int J
765 Parasitol. 2010;40(4):453-62. Epub 20091029. doi: 10.1016/j.ijpara.2009.09.008.
766 PubMed PMID: 19837073.
767 21. Dey G, Culley S, Curran S, Schmidt U, Henriques R, Kukulski W, et al. Closed mitosis
768 requires local disassembly of the nuclear envelope. Nature. 2020;585(7823):119-23.
769 Epub 20200826. doi: 10.1038/s41586-020-2648-3. PubMed PMID: 32848252; PubMed
770 Central PMCID: PMCPMC7610560.
771 22. Matthews H, Duffy CW, Merrick CJ. Checks and balances? DNA replication and the cell
772 cycle in Plasmodium. Parasit Vectors. 2018;11(1):216. Epub 20180327. doi:
773 10.1186/s13071-018-2800-1. PubMed PMID: 29587837; PubMed Central PMCID:
774 PMCPMC5872521.
775 23. Rout MP, Obado SO, Schenkman S, Field MC. Specialising the parasite nucleus: Pores,
776 lamins, chromatin, and diversity. PLoS Pathog. 2017;13(3):e1006170. Epub 20170302.
777 doi: 10.1371/journal.ppat.1006170. PubMed PMID: 28253370; PubMed Central PMCID:
778 PMCPMC5333908.
779 24. Suvorova ES, Francia M, Striepen B, White MW. A novel bipartite centrosome coordinates
780 the apicomplexan cell cycle. PLoS Biol. 2015;13(3):e1002093. Epub 20150303. doi:
781 10.1371/journal.pbio.1002093. PubMed PMID: 25734885; PubMed Central PMCID:
782 PMCPMC4348508.

783 25. Chen CT, Kelly M, Leon J, Nwagbara B, Ebbert P, Ferguson DJ, et al. Compartmentalized
784 Toxoplasma EB1 bundles spindle microtubules to secure accurate chromosome
785 segregation. Mol Biol Cell. 2015;26(25):4562-76. Epub 20151014. doi:
786 10.1091/mbc.E15-06-0437. PubMed PMID: 26466679; PubMed Central PMCID:
787 PMCPMC4678015.
788 26. Hoeijmakers WA, Flueck C, Francoijs KJ, Smits AH, Wetzel J, Volz JC, et al. Plasmodium
789 falciparum centromeres display a unique epigenetic makeup and cluster prior to and
790 during schizogony. Cell Microbiol. 2012;14(9):1391-401. Epub 20120515. doi:
791 10.1111/j.1462-5822.2012.01803.x. PubMed PMID: 22507744.
792 27. Brooks CF, Francia ME, Gissot M, Croken MM, Kim K, Striepen B. Toxoplasma gondii
793 sequesters centromeres to a specific nuclear region throughout the cell cycle. Proc Natl
794 Acad Sci U S A. 2011;108(9):3767-72. Epub 20110214. doi: 10.1073/pnas.1006741108.
795 PubMed PMID: 21321216; PubMed Central PMCID: PMCPMC3048097.
796 28. Arnot DE, Ronander E, Bengtsson DC. The progression of the intra-erythrocytic cell cycle of
797 Plasmodium falciparum and the role of the centriolar plaques in asynchronous mitotic
798 division during schizogony. Int J Parasitol. 2011;41(1):71-80. Epub 20100917. doi:
799 10.1016/j.ijpara.2010.07.012. PubMed PMID: 20816844.
800 29. Iwanaga S, Khan SM, Kaneko I, Christodoulou Z, Newbold C, Yuda M, et al. Functional
801 identification of the Plasmodium centromere and generation of a Plasmodium artificial
802 chromosome. Cell Host Microbe. 2010;7(3):245-55. doi: 10.1016/j.chom.2010.02.010.
803 PubMed PMID: 20227667; PubMed Central PMCID: PMCPMC2996609.
804 30. Absalon S. A dynamic barrier: remodeling of the nuclear envelope during closed mitosis in
805 malaria parasites. mSphere. 2025;10(7):e0099924. Epub 20250609. doi:
806 10.1128/msphere.00999-24. PubMed PMID: 40488521; PubMed Central PMCID:
807 PMCPMC12306155.
808 31. Weiner A, Dahan-Pasternak N, Shimoni E, Shinder V, von Huth P, Elbaum M, et al. 3D
809 nuclear architecture reveals coupled cell cycle dynamics of chromatin and nuclear pores
810 in the malaria parasite Plasmodium falciparum. Cell Microbiol. 2011;13(7):967-77. Epub
811 20110428. doi: 10.1111/j.1462-5822.2011.01592.x. PubMed PMID: 21501361.
812 32. Francia ME, Striepen B. Cell division in apicomplexan parasites. Nat Rev Microbiol.
813 2014;12(2):125-36. Epub 20140102. doi: 10.1038/nrmicro3184. PubMed PMID:
814 24384598.
815 33. Kursel LE, Malik HS. Centromeres. Curr Biol. 2016;26(12):R487-R90. doi:
816 10.1016/j.cub.2016.05.031. PubMed PMID: 27326706.
817 34. Hegemann JH, Fleig UN. The centromere of budding yeast. Bioessays. 1993;15(7):451-60.
818 doi: 10.1002/bies.950150704. PubMed PMID: 8379948.
819 35. Kelly JM, McRobert L, Baker DA. Evidence on the chromosomal location of centromeric
820 DNA in Plasmodium falciparum from etoposide-mediated topoisomerase-II cleavage.
821 Proc Natl Acad Sci U S A. 2006;103(17):6706-11. Epub 20060414. doi:
822 10.1073/pnas.0510363103. PubMed PMID: 16617116; PubMed Central PMCID:
823 PMCPMC1458945.
824 36. Viera A, Page J, Rufas JS. Inverted meiosis: the true bugs as a model to study. Genome Dyn.
825 2009;5:137-56. doi: 10.1159/000166639. PubMed PMID: 18948713.
826 37. Mandrioli M, Manicardi GC. Holocentric chromosomes. PLoS Genet. 2020;16(7):e1008918.
827 Epub 20200730. doi: 10.1371/journal.pgen.1008918. PubMed PMID: 32730246;
828 PubMed Central PMCID: PMCPMC7392213.

829 38. Marques A, Drinnenberg IA. Same but different: Centromere regulations in holocentric
830 insects and plants. Curr Opin Cell Biol. 2025;93:102484. Epub 20250220. doi:
831 10.1016/j.ceb.2025.102484. PubMed PMID: 39983583.
832 39. Bensasson D. Evidence for a high mutation rate at rapidly evolving yeast centromeres. BMC
833 Evol Biol. 2011;11:211. Epub 20110718. doi: 10.1186/1471-2148-11-211. PubMed
834 PMID: 21767380; PubMed Central PMCID: PMCPMC3155921.
835 40. Csink AK, Henikoff S. Something from nothing: the evolution and utility of satellite repeats.
836 Trends Genet. 1998;14(5):200-4. doi: 10.1016/s0168-9525(98)01444-9. PubMed PMID:
837 9613205.
838 41. Talbert PB, Henikoff S. Centromeres drive and take a break. Chromosome Res.
839 2025;33(1):17. Epub 20250804. doi: 10.1007/s10577-025-09777-z. PubMed PMID:
840 40759764; PubMed Central PMCID: PMCPMC12321929.
841 42. Henikoff S, Ahmad K, Malik HS. The centromere paradox: stable inheritance with rapidly
842 evolving DNA. Science. 2001;293(5532):1098-102. doi: 10.1126/science.1062939.
843 PubMed PMID: 11498581.
844 43. Talbert PB, Henikoff S. What makes a centromere? Exp Cell Res. 2020;389(2):111895. Epub
845 20200206. doi: 10.1016/j.yexcr.2020.111895. PubMed PMID: 32035948.
846 44. Skene PJ, Henikoff S. An efficient targeted nuclease strategy for high-resolution mapping of
847 DNA binding sites. Elife. 2017;6. Epub 20170116. doi: 10.7554/eLife.21856. PubMed
848 PMID: 28079019; PubMed Central PMCID: PMCPMC5310842.
849 45. Herrera-Solorio AM, Vembar SS, MacPherson CR, Lozano-Amado D, Meza GR,
850 Xoconostle-Cazares B, et al. Clipped histone H3 is integrated into nucleosomes of DNA
851 replication genes in the human malaria parasite Plasmodium falciparum. EMBO Rep.
852 2019;20(4). Epub 20190304. doi: 10.15252/embr.201846331. PubMed PMID: 30833341;
853 PubMed Central PMCID: PMCPMC6446197.
854 46. Verma G, Surolia N. Plasmodium falciparum CENH3 is able to functionally complement
855 Cse4p and its, C-terminus is essential for centromere function. Mol Biochem Parasitol.
856 2013;192(1-2):21-9. Epub 20131206. doi: 10.1016/j.molbiopara.2013.11.002. PubMed
857 PMID: 24316361.
858 47. Naumov A, Kratzer S, Ting LM, Kim K, Suvorova ES, White MW. The Toxoplasma
859 Centrocone Houses Cell Cycle Regulatory Factors. mBio. 2017;8(4). Epub 20170822.
860 doi: 10.1128/mBio.00579-17. PubMed PMID: 28830940; PubMed Central PMCID:
861 PMCPMC5565962.
862 48. Mahajan B, Selvapandiyan A, Gerald NJ, Majam V, Zheng H, Wickramarachchi T, et al.
863 Centrins, cell cycle regulation proteins in human malaria parasite Plasmodium
864 falciparum. J Biol Chem. 2008;283(46):31871-83. Epub 20080808. doi:
865 10.1074/jbc.M800028200. PubMed PMID: 18693242.
866 49. Liu C, Wang L, Lancto CA, Abrahamsen MS. Characterization of a Cryptosporidium parvum
867 protein that binds single-stranded G-strand telomeric DNA. Mol Biochem Parasitol.
868 2009;165(2):132-41. Epub 20090204. doi: 10.1016/j.molbiopara.2009.01.013. PubMed
869 PMID: 19428660.
870 50. Ay F, Bunnik EM, Varoquaux N, Bol SM, Prudhomme J, Vert JP, et al. Three-dimensional
871 modeling of the P. falciparum genome during the erythrocytic cycle reveals a strong
872 connection between genome architecture and gene expression. Genome Res.
873 2014;24(6):974-88. Epub 20140326. doi: 10.1101/gr.169417.113. PubMed PMID:
874 24671853; PubMed Central PMCID: PMCPMC4032861.

875 51. Bunnik EM, Cook KB, Varoquaux N, Batugedara G, Prudhomme J, Cort A, et al. Changes in
876 genome organization of parasite-specific gene families during the Plasmodium
877 transmission stages. Nat Commun. 2018;9(1):1910. Epub 20180515. doi:
878 10.1038/s41467-018-04295-5. PubMed PMID: 29765020; PubMed Central PMCID:
879 PMCPMC5954139.
880 52. Hollin T, Le Roch KG. From Genes to Transcripts, a Tightly Regulated Journey in
881 Plasmodium. Front Cell Infect Microbiol. 2020;10:618454. Epub 20201217. doi:
882 10.3389/fcimb.2020.618454. PubMed PMID: 33425787; PubMed Central PMCID:
883 PMCPMC7793691.
884 53. McIntosh JR. Mitosis. Cold Spring Harb Perspect Biol. 2016;8(9). Epub 20160901. doi:
885 10.1101/cshperspect.a023218. PubMed PMID: 27587616; PubMed Central PMCID:
886 PMCPMC5008068.
887 54. Perez-Cadahia B, Drobic B, Davie JR. H3 phosphorylation: dual role in mitosis and
888 interphase. Biochem Cell Biol. 2009;87(5):695-709. doi: 10.1139/O09-053. PubMed
889 PMID: 19898522.
890 55. Gerald N, Mahajan B, Kumar S. Mitosis in the human malaria parasite Plasmodium
891 falciparum. Eukaryot Cell. 2011;10(4):474-82. Epub 20110211. doi: 10.1128/EC.00314-
892 10. PubMed PMID: 21317311; PubMed Central PMCID: PMCPMC3127633.
893 56. Steiner FA, Henikoff S. Holocentromeres are dispersed point centromeres localized at
894 transcription factor hotspots. Elife. 2014;3:e02025. Epub 20140101. doi:
895 10.7554/eLife.02025. PubMed PMID: 24714495; PubMed Central PMCID:
896 PMCPMC3975580.
897 57. Xia J, Venkat A, Bainbridge RE, Reese ML, Le Roch KG, Ay F, et al. Third-generation
898 sequencing revises the molecular karyotype for Toxoplasma gondii and identifies
899 emerging copy number variants in sexual recombinants. Genome Res. 2021;31(5):834-
900 51. Epub 20210427. doi: 10.1101/gr.262816.120. PubMed PMID: 33906962; PubMed
901 Central PMCID: PMCPMC8092015.
902 58. Blauwkamp J, Ambekar SV, Hussain T, Mair GR, Beck JR, Absalon S. Nuclear pore
903 complexes undergo Nup221 exchange during blood-stage asexual replication of parasites.
904 Msphere. 2024;9(12). doi: 10.1128/msphere.00750-24. PubMed PMID:
905 WOS:001352594000001.
906 59. Edwards-Smallbone J, Jensen AL, Roberts LE, Totanes FIG, Hart SR, Merrick CJ.
907 Plasmodium falciparum GBP2 Is a Telomere-Associated Protein That Binds to G-
908 Quadruplex DNA and RNA. Front Cell Infect Microbiol. 2022;12:782537. Epub
909 20220222. doi: 10.3389/fcimb.2022.782537. PubMed PMID: 35273922; PubMed Central
910 PMCID: PMCPMC8902816.
911 60. Zhao N, Gong P, Li Z, Cheng B, Li J, Yang Z, et al. Identification of a telomeric DNA-
912 binding protein in Eimeria tenella. Biochem Biophys Res Commun. 2014;451(4):599-
913 602. Epub 20140813. doi: 10.1016/j.bbrc.2014.08.030. PubMed PMID: 25128826.
914 61. Melters DP, Paliulis LV, Korf IF, Chan SW. Holocentric chromosomes: convergent
915 evolution, meiotic adaptations, and genomic analysis. Chromosome Res. 2012;20(5):579-
916 93. doi: 10.1007/s10577-012-9292-1. PubMed PMID: 22766638.
917 62. Lucek K, Augustijnen H, Escudero M. A holocentric twist to chromosomal speciation?
918 Trends Ecol Evol. 2022;37(8):655-62. Epub 20220426. doi: 10.1016/j.tree.2022.04.002.
919 PubMed PMID: 35484024.

920 63. Funkhouser-Jones LJ, Xu R, Wilke G, Fu Y, Schriefer LA, Makimaa H, et al. Microbiota-
921 produced indole metabolites disrupt mitochondrial function and inhibit Cryptosporidium
922 parvum growth. Cell Rep. 2023;42(7):112680. Epub 2023/06/29. doi:
923 10.1016/j.celrep.2023.112680. PubMed PMID: 37384526.
924 64. Pardy RD, Wallbank BA, Striepen B, Hunter CA. Immunity to Cryptosporidium: insights
925 into principles of enteric responses to infection. Nat Rev Immunol. 2024;24(2):142-55.
926 Epub 20230911. doi: 10.1038/s41577-023-00932-3. PubMed PMID: 37697084.
927 65. Martinez-Perez E, Schvarzstein M, Barroso C, Lightfoot J, Dernburg AF, Villeneuve AM.
928 Crossovers trigger a remodeling of meiotic chromosome axis composition that is linked
929 to two-step loss of sister chromatid cohesion. Genes Dev. 2008;22(20):2886-901. doi:
930 10.1101/gad.1694108. PubMed PMID: 18923085; PubMed Central PMCID:
931 PMCPMC2569886.
932 66. Kimball A, Funkhouser-Jones L, Huang W, Xu R, Witola WH, Sibley LD. Mendelian
933 segregation and high recombination rates facilitate genetic analyses in Cryptosporidium
934 parvum. PLoS Genet. 2024;20(6):e1011162. Epub 20240617. doi:
935 10.1371/journal.pgen.1011162. PubMed PMID: 38885280; PubMed Central PMCID:
936 PMCPMC11213348.
937 67. Wilke G, Ravindran S, Funkhouser-Jones L, Barks J, Wang Q, VanDussen KL, et al.
938 Monoclonal antibodies to intracellular stages of *Cryptosporidium parvum* define life
939 cycle progression in vitro. Msphere. 2018;3(3):e00124-18. Epub 2018/06/01. doi:
940 10.1128/mSphere.00124-18. PubMed PMID: 29848759; PubMed Central PMCID:
941 PMCPMC5976880.
942 68. Xu R, Beatty WL, Greigert V, Witola WH, Sibley LD. Multiple pathways for glucose
943 phosphate transport and utilization support growth of Cryptosporidium parvum. Nat
944 Commun. 2024;15(1):380. Epub 20240109. doi: 10.1038/s41467-024-44696-3. PubMed
945 PMID: 38191884; PubMed Central PMCID: PMCPMC10774378.
946 69. Wilke G, Funkhouser-Jones L, Wang Y, Ravindran S, Wang Q, Beatty WL, et al. Forward
947 genetics in *Cryptosporidium* enabled by complete in vitro development in stem cell-
948 derived intestinal epithlium. Cell Host Microbe. 2019;doi.org/10.2139/ssrn.3331307.
949 70. Xu R, Beatty WL, Greigert V, Witola WH, Sibley LD. Multiple pathways for glucose
950 phosphate transport and utilization support growth of Cryptosporidium parvum. bioRxiv.
951 2023. Epub 2023/07/10. doi: 10.1101/2023.06.27.546703. PubMed PMID: 37425855;
952 PubMed Central PMCID: PMCPMC10327089.
953 71. Akey ME, Xu R, Ravindran S, Funkhouser-Jones L, Sibley LD. Apical Secretory
954 Glycoprotein Complex Contributes to Cell Attachment and Entry by Cryptosporidium
955 parvum. mBio. 2023;14(1):e0306422. Epub 2023/02/02. doi: 10.1128/mbio.03064-22.
956 PubMed PMID: 36722968; PubMed Central PMCID: PMCPMC9973360.
957 72. Xu R, Feng Y, Xiao L, Sibley LD. Insulinase-like Protease 1 Contributes to Macrogamont
958 Formation in Cryptosporidium parvum. mBio. 2021;12(2). Epub 2021/03/11. doi:
959 10.1128/mBio.03405-20. PubMed PMID: 33688009; PubMed Central PMCID:
960 PMCPMC8092296.
961 73. Kuhlenschmidt TB, Rutaganira FU, Long S, Tang K, Shokat KM, Kuhlenschmidt MS, et al.
962 Inhibition of Calcium-Dependent Protein Kinase 1 (CDPK1) In Vitro by
963 Pyrazolopyrimidine Derivatives Does Not Correlate with Sensitivity of Cryptosporidium
964 parvum Growth in Cell Culture. Antimicrob Agents Chemother. 2015;60(1):570-9.

965 74. Current WL. Techniques and laboratory maintenance of *Cryptosporidium*. In: Dubey JP,
966 Speer CA, Fayer R, editors. Cryptosporidiosis of Man and Animals. Boca Raton, FL:
967 CRC Press; 1990. p. 44-77.
968 75. Mehta S, Sibley LD. Actin depolymerizing factor controls actin turnover and gliding motility
969 in Toxoplasma gondii. Mol Biol Cell. 2011;22(8):1290-9. Epub 20110223. doi:
970 10.1091/mbc.E10-12-0939. PubMed PMID: 21346192; PubMed Central PMCID:
971 PMCPMC3078074.
972 76. Behnke MS, Radke JB, Smith AT, Sullivan WJ, Jr., White MW. The transcription of
973 bradyzoite genes in Toxoplasma gondii is controlled by autonomous promoter elements.
974 Mol Microbiol. 2008;68(6):1502-18. Epub 20080421. doi: 10.1111/j.1365-
975 2958.2008.06249.x. PubMed PMID: 18433450; PubMed Central PMCID:
976 PMCPMC2440561.
977 77. Waldman BS, Schwarz D, Wadsworth MH, 2nd, Saeij JP, Shalek AK, Lourido S.
978 Identification of a Master Regulator of Differentiation in Toxoplasma. Cell.
979 2020;180(2):359-72 e16. Epub 20200116. doi: 10.1016/j.cell.2019.12.013. PubMed
980 PMID: 31955846; PubMed Central PMCID: PMCPMC6978799.
981 78. Huang W, Tang K, Chen C, Arrowood MJ, Chen M, Guo Y, et al. Sequence introgression
982 from exogenous lineages underlies genomic and biological differences among
983 Cryptosporidium parvum IOWA lines. Water Res. 2024;254:121333. Epub 20240217.
984 doi: 10.1016/j.watres.2024.121333. PubMed PMID: 38402753; PubMed Central PMCID:
985 PMCPMC10994760.
986

987

988

989 **Supporting Information**

990 **S1 Table.** Transgenic *Cryptosporidium* strains used in this study.

991 **S2 Table.** Key Resources used in the experiments.

992 **S3 Table.** Oligonucleotides and plasmids used in this study.

993

994 **S1 Dataset** Information of sequencing samples from the Cut&Run and summary statistics of the

995 data.

996 **S2 Dataset** Genomic location of the CENH3 sites within coding regions.

997 **S3 Dataset** Genomic location of the CENH3 sites within intergenic regions.

998